

FOURIER MODELING OF THE RADIO TORUS SURROUNDING SUPERNOVA 1987A

C.-Y. Ng¹, B. M. Gaensler^{1,a}, L. Staveley-Smith^{2,b}, R. N. Manchester^{3,a}, M. J. Kesteven³,
L. Ball³ and A. K. Tzioumis³

ncy@physics.usyd.edu.au

ABSTRACT

We present detailed Fourier modeling of the radio remnant of Supernova 1987A, using high-resolution 9 GHz and 18 GHz data taken with the Australia Telescope Compact Array over the period 1992 to 2008. We develop a parameterized three-dimensional torus model for the expanding radio shell, in which the emission is confined to an inclined equatorial belt; our model also incorporates both a correction for light travel-time effects and an overall east-west gradient in the radio emissivity. By deriving an analytic expression for the two-dimensional Fourier transform of the projected three-dimensional brightness distribution, we can fit our spatial model directly to the interferometric visibility data. This provides robust estimates to the radio morphology at each epoch. The best-fit results suggest a constant remnant expansion at $4000 \pm 400 \text{ km s}^{-1}$ over the 16-year period covered by the observations. The model fits also indicate substantial mid-latitude emission, extending to $\pm 40^\circ$ on either side of the equatorial plane. This likely corresponds to the extra-planar structure seen in $\text{H}\alpha$ and $\text{Ly}\alpha$ emission from the supernova reverse shock, and broadly supports hydrodynamic models in which the complex circumstellar environment was produced by a progression of interacting winds from the progenitor. Our model quantifies the clear asymmetry seen in the radio images: we find that the eastern half of the radio remnant is consistently $\sim 40\%$ brighter than the western half at all epochs, which may result from an asymmetry in the ejecta distribution between these two hemispheres.

¹Institute of Astronomy, School of Physics, The University of Sydney, Sydney NSW, Australia

²School of Physics, The University of Western Australia, Crawley WA, Australia

³Australia Telescope National Facility, CSIRO, Marsfield NSW, Australia

^aARC Federation Fellow

^bPremier's Fellow in Radio Astronomy

Subject headings: circumstellar matter - radio continuum: ISM - shock waves - supernovae:individual (SN 1987A) - supernova remnants - techniques: interferometric

1. Introduction

Supernova (SN) 1987A in the Large Magellanic Cloud (at a distance of 51 kpc) was the nearest supernova observed in almost 400 years, and has enabled detailed studies of supernova physics. The detection of neutrino bursts indicated that the event was a core collapse, however SN 1987A was not a typical example of a type II supernova in many aspects. Optical observations revealed a triple-ring nebula surrounding the explosion (Burrows et al. 1995). This indicates the inner surface of the densest circumstellar material (CSM) that was ionized by the supernova UV flash. Observations of the light echos provided a more comprehensive picture of the structure (Sugerman et al. 2005a,b). The CSM was found to have a peanut-like bipolar geometry, inclined at 43° to the line of sight.

The complex circumstellar environment can be understood as analogous to the interacting stellar wind model, as originally proposed to explain planetary nebulae (Kwok 1982). The progenitor star of SN 1987A, Sk $-69^\circ 202$, is believed to have evolved from a red supergiant (RSG) to a blue supergiant (BSG) about 20000 years before core collapse (Crotts & Heathcote 1991). After the transition, the fast, low density BSG wind overran the slow, dense RSG wind and swept it into a circumstellar shell. Some models suggest that the RSG wind could have been highly aspherical, due to a binary merger (Morris & Podsiadlowski 2007) or to equatorial wind compression (Collins et al. 1999). Hydrodynamic simulations of the subsequent interaction between the stellar outflow can reproduce the overall bipolar CSM structure and can possibly explain the origin of the triple-ring nebula (Blondin & Lundqvist 1993; Martin & Arnett 1995; Morris & Podsiadlowski 2007).

At radio frequencies, an initial outburst from SN 1987A peaked on day 4 and then decayed rapidly (Turtle et al. 1987). The radio emission was redetected again in mid-1990 by the Molonglo Observatory Synthesis Telescope (MOST) (Turtle et al. 1990) and then by the Australia Telescope Compact Array (ATCA) (Staveley-Smith et al. 1992). Long term monitoring has shown a monotonic increase in the radio flux since the reappearance (Staveley-Smith et al. 2007). This is believed to be synchrotron radiation from the continuous injection of nonthermal particles as the blast wave expands into the CSM. In this general picture, electrons are accelerated to ultrarelativistic velocities by the shock and

then interact with the magnetic field that is amplified by the Rayleigh-Taylor instability near the contact discontinuity (Jun & Norman 1996). Therefore the radio emission is expected to be generated between the forward and reverse shocks. A detailed time-dependent model of diffusive shock acceleration for SN 1987A was first discussed by Ball & Kirk (1992). Duffy et al. (1995) further improved the model by considering the accelerated ions that heat the upstream plasma and modify the shock front. Chevalier & Dwarkadas (1995) slightly modified the physical picture and attributed the radio emission to the interaction between the ejecta and an HII region located inside the optical ring. In this model, the HII region is a shell of swept-up RSG wind photoionized by the BSG. The ongoing encounter between the shock and CSM also predicts a steady increase in X-ray emission, which has been confirmed by long term X-ray monitoring (Park et al. 2007). Moreover, it was suggested by Chevalier & Dwarkadas (1995) that the HII region would delay the encounter of the blast wave with the optical ring to 2005 ± 3 CE. By then, there was predicted to be a drastic increase in the radio flux.

From an energetic point of view, generation of the radio emission requires much less energy compared to other wavebands such as optical and X-ray. Hence, radio data are a sensitive tracer of the shock interaction. As the supernova ejecta expand into the CSM, the radio morphology will follow the evolution of the forward and reverse shocks and traces out the global structure of the dense CSM. High resolution imaging observations with the ATCA have been performed since mid-1991 (Staveley-Smith et al. 1993a). Fig. 1 shows the diffraction-limited images at 9 GHz. With an angular resolution of $0''.9$, these images already reveal the spatially extended structure of SN 1987A. Briggs (1994) and Staveley-Smith et al. (1993a) tested and employed the super-resolution to further improve the resolution to $0''.4$ and found that the remnant has a limb-brightened shell morphology (Fig. 2). Applying the same technique to observations in 1992-1995, Gaensler et al. (1997) discovered two bright lobes in the shell. The lobes were aligned along the major axis of the optical ring and the eastern lobe was about 1.2-1.8 times brighter than the western lobe. The ATCA 18 GHz upgrade provided twice the angular resolution as at 9 GHz, and confirmed all these structures in diffraction-limited images (Manchester et al. 2005). The 18 GHz image is well described by an inclined thick equatorial ring with the same orientation as the bipolar CSM. Recently, Tingay et al. (2008, in preparation) performed a new VLBI observation of SN 1987A. The 1.4 GHz image similarly shows two lobes coincident with the ones in the 9 and 18 GHz images. In the hard X-ray band, a thick ring morphology has also been observed (Park et al. 2002), suggesting a similar emission process as at radio frequency. However, the optical hot spots, which are the inward protruding dense gas shocked by the blast wave (Pun et al. 2002; Sugerman et al. 2002), show no correlation to the radio lobes in position (Manchester et al. 2002). Although the emergence of the optical hot spots coincided with the arrival of the radio-producing shock

at those regions (Ball et al. 2001), Manchester et al. (2002) indicate that this had little effect on the morphology of the radio remnant.

As in many astrophysical observations, quantitative measurements of the physical parameters require careful data modeling (e.g. Ng & Romani 2008). In our case, Staveley-Smith et al. (1993b) demonstrated that a robust way to obtain the remnant size is to model the visibility data directly in the u - v plane. They performed two dimensional (2D) Fourier transform of a range of models including a spherical shell and a thin ring and then fitted them to the visibility data to measure the remnant’s expansion. Gaensler et al. (1997) employed a thin spherical shell model in the fit and found a mean expansion velocity of $\sim 3000 \text{ km s}^{-1}$ between 1992-1995. Later, Manchester et al. (2002) improved the modeling by adding two point sources to the thin shell model to account for the eastern and western lobes as observed. Recently, Gaensler et al. (2007) applied the thin shell model to fit all 9 GHz observations from 1992 to 2006 and suggested a gradual acceleration in the expansion followed by a recent deceleration.

The ATCA imaging campaign has the longest time span for monitoring of SN 1987A at any wavelength. With more than 17 years of observations from a single instrument, we are now ready to improve the modeling. In this paper, we develop a better model to account for more features in the remnant. We will model the observed east-west asymmetry as well as the expected light travel time effects. The fits to all the 9 GHz and 18 GHz observations from 1992-2008 can then provide a better understanding of the structure and evolution of SN 1987A. We describe the ATCA observations and data reduction in §2, then the detailed modeling and fitting procedures in §3. The results and discussion are presented in §§4 and 5. Detailed mathematics of the model is listed Appendix A.

2. Observations

The ATCA is a radio interferometer consisting of six 22-m dishes on a 6-km track, located near Narrabri, NSW, Australia (Frater et al. 1992). The ATCA observations of SN 1987A discussed here were performed at 9 and 18 GHz with 6 km array configurations. At 9 GHz, the source was observed approximately every six months with long integration times (6-12 hr) at two simultaneous frequencies in the range 8.6 to 9.1 GHz. In the observations, the phase center was placed $10''$ south of the remnant to avoid any possible artifacts (Ekers 1999). Detailed observational parameters of all the datasets used in this study are listed in Table 1. Two ATCA 18 GHz observations are included in the analysis. Each was taken one day before or after a 9 GHz observation, thus allowing a direct comparison between the two frequency bands. Except for the last epoch, a preliminary analysis of all the 9 and 18 GHz

data has been presented in Gaensler et al. (2007).

The data reduction was carried out with the *MIRIAD* package (Sault et al. 1995). We examined the data carefully for bad points and rejected scans during poor atmospheric phase stability. From 1996 onwards, the source has sufficient signal-to-noise ratio (S/N) to allow phase self-calibration, which was performed with a 5 minute solution interval time. This time scale is long enough to integrate an appreciable S/N, but is short enough to track the atmospheric phase variations. The phase self-calibration results in a significant improvement in the fidelity of the complex gains for each antenna. After the calibration, we shifted the phase center to the supernova site and then averaged the visibility data in 5 minute intervals. Again, this is long enough to obtain good S/N on each baseline, but is short enough to track the structure of the source. We note that there is negligible loss in amplitude due to time-averaging of the data, because the source is of small angular extent and has been shifted to the phase center (Bridle & Schwab 1999).

3. Modeling

Figures 1 and 2 show the diffraction-limited and super-resolved images, respectively, of the 9 GHz observations; some epochs were averaged together to boost the S/N (see Table 1). Following the procedures described by Gaensler et al. (1997), the dirty maps were first generated from the calibrated visibility data, then deconvolved using a maximum entropy (MEM) algorithm (Gull & Daniell 1978). The MEM model was then convolved with a diffraction-limited beam and a super-resolved circular beam with FWHM $0''.4$ for Fig. 1 and 2, respectively. Finally the models were combined with the unscaled residuals and then regridded at a pixel scale of $0''.01$. The structure observed in the super-resolved 9 GHz images is confirmed by the 18 GHz diffraction-limited images (see Fig. 1 in Manchester et al. 2005, and Fig. 9 of this paper), showing a morphology that is well-described by an inclined thick ring. Based on the surface brightness at the center of the ring, Manchester et al. (2005) argued that the radio morphology sits somewhere between a spherical shell and an equatorial ring.

Motivated by all these results, we below present a generic inclined torus model to capture the overall structure of the radio emission. We emphasize that our model is a simplified picture of the physical situation and that we have not attempted to reproduce every single detail of the emission. Instead, this study aims to obtain characteristic scales of the emission, such as the size and height of the emitting region, and the evolution of these parameters with time.

3.1. Equatorial Belt Torus Model

The extra-planar structure of SN 1987A mentioned above obviously does not fit into the simple picture of a spherical shell or a 2D ring, but is better described by a 3D torus with a finite thickness. To incorporate these features, we propose an equatorial belt torus model, i.e. a spherical shell truncated at arbitrary latitude. This gives a continuous variation between a ring and a spherical shell geometry. Fig. 3 illustrates this model. It is a truncated optically thin shell with uniform emissivity and inclined to the observer line of sight. The geometry is specified by the radius R (averaged between the inner and outer shells), the shock thickness δ (as a fraction of R) and the half opening angle θ . Additional parameters include the flux density f_0 , center position (x_0, y_0) , inclination ζ and position angle (P.A.) Ψ on the plane of the sky. In the limiting case of $\theta = 0^\circ$, the torus is reduced to an equatorial ring, while $\theta = 90^\circ$ gives a spherical shell. The east-west asymmetry of the remnant is modeled by a linear gradient in the torus emissivity across the equatorial plane (not in the plane of the sky). Hence two more parameters are introduced: the magnitude g and the P.A. ϕ of the gradient. The former is normalized to the fractional change in flux density at R , and the gradient direction is defined from the brightest point towards the faintest point, with the P.A. measured from the projected observer line of sight (see Fig. 3). Finally, we correct for light travel time effects. Since the remnant flux is increasing, the north rim, which is about a light year closer to the Earth than the south, appears brighter. Also due to the finite speed of light, expansion of the remnant distorts the torus and shifts its center to the north. To derive corrections for both effects, we employed linear approximations to the expansion and light curve locally at each epoch, with the rate of change determined from the results of Gaensler et al. (2007) and Staveley-Smith et al. (2007). We found that the north rim is at most 20% brighter than the south as a result of the light travel effects. On the other hand, the effects of expansion are only of second order, at the level of less than 1%. Therefore, the latter will be ignored throughout the following analysis. A detailed mathematical description of the torus model and light travel time effects is given in Appendix A.

3.2. Fitting Procedure

Staveley-Smith et al. (1993b) showed that a robust way to estimate the remnant's geometry is to model the visibility data directly in the u - v domain, for which the measurement errors are uncorrelated and the fitting is not complicated by the deconvolution process. In order to do that, we first have to derive a 2D Fourier transform for the inclined torus model. This was achieved by building up the model torus from thin rings, which can be transformed to Fourier space analytically via the Hankel transform (Bracewell 2000). The linear gradi-

ents in the model, including the asymmetry and light travel time correction, are transformed using the convolution theorem and are turned into derivatives in the u - v domain. Putting these together, we obtain an analytic expression of the torus model under a Fourier transform (see Appendix A for the detailed formulae).

Once the model is established, the fitting procedure is by the minimization of

$$\chi^2 = \sum \left| \frac{\text{vis}(u, v) - \text{model}(u, v)}{\sigma(u, v)} \right|^2,$$

where σ is the statistical uncertainty associated with each measurement. Given that the rms noise levels in our final images is close to the thermal noise of the antenna receivers, we argue that other sources of errors in the measurement, including the systematic errors due to the calibration or instrumental effects are negligible. The χ^2 minimization is carried out by the task `uvfit` in *MIRIAD*, with modifications to the code for the torus model. As discussed, the symmetry axis of the system has been well measured from optical observations of the triple-ring system and of light echoes (Sugerman et al. 2005b; Pun 2007). Therefore, we fixed the orientation of the torus during the fit, by adopting the values $\Psi = -7.6$ and $\zeta = 43.4$ from Pun (2007). The uncertainties in the fits were estimated through a bootstrapping method (Efron & Tibshirani 1993), since the errors in the fits are likely to be non-Gaussian. Following the procedure described in Press et al. (1992), bootstrap samples were generated by randomly drawing the visibility measurements from an observation, with replacement. After the same number of visibilities as the data have been drawn, the bootstrap replica is fitted with the same procedure to obtain the torus parameters. For each observation, we fitted 2000 bootstrap iterations, and the 68% intervals for each parameter’s distribution are quoted throughout as the 1σ uncertainty. This gives the projection of multi-dimensional errors that accounts for the correlations between fitting parameters. As the S/N in the observations increases towards the later epochs, the parameter uncertainties due to measurement errors become negligible and the systematic errors in the modeling dominate. In the real world, the detailed structure of SN 1987A is much more complicated than what our simple model can capture, resulting in systematic errors in the fits. We have attempted to quantify this term for the radius, which is the parameter we are most interested in. Since the exact structure of the remnant is unknown, the radius measurement is always model-dependent. Similar to Manchester et al. (2002), we fitted the 9 GHz observations to various plausible models, including a spherical shell and a shell plus two point sources. In general, these fits obtain slightly different values of R and hence the variation provides a handle of the systematic errors in the modeling.

4. Results

4.1. 9 GHz Observations

The best-fit torus parameters are listed in Table 2 and plotted in Fig. 5. Most of the fits to the ATCA 9 GHz data are robust, except for a few epochs with very large χ^2 values that are possibly due to poor calibration. The fits are generally better towards the late epochs, however as shown in Table 2, the typical reduced χ^2 value is ~ 1.5 . This is still relatively large, suggesting that our model is not a perfect fit to the observations, and that there are unmodeled features in the data which contribute to the systematic residuals. This result is not unexpected since the model aims to capture only the characteristic features of the emission, rather than reproducing every small-scale structure. Nevertheless, our model does provide a better description to the data than a simple thin spherical shell model used in previous studies (Gaensler et al. 1997, 2007; Manchester et al. 2002). Fig. 4 plots the visibilities of the data and models along two orthogonal axes in the u - v domain. The difference between a torus and a spherical shell models is obvious, in particular along the u -axis, because this direction corresponds to east-west in the sky, where the radio emission shows large asymmetry. The plots clearly indicate that the asymmetric torus model is a better fit over a simple shell, and, at least to the first order, well describes the east-west asymmetry. On the other hand, we note that a similar plot with azimuthally averaged u - v data (Fig. 6 in Gaensler et al. 2007) masks the discrepancy between the data and a simple shell model. To provide a quantitative comparison between different models, we have reproduced the fits with a thin shell model and a thin spherical shell plus two points model as in Manchester et al. (2002). Table 3 shows that the torus fit always provides lower χ^2/ν values than the shell fit. The shell plus two points model and the torus model have comparable goodness-of-fit, but the former requires two more fitting parameters. Therefore, we conclude that our torus model is a substantial improvement over the simple models used previously.

Although we did not attempt to provide a physical model to interpret the observed radio light curve, we note that the fluxes obtained from the fits are consistent with the values reported by Staveley-Smith et al. (2007). In the following discussions, we will concentrate on the torus geometry.

Fig. 6 shows the best-fit model for epoch 2008.0, with the left panel illustrating the model at very high spatial resolution. The images were generated in the u - v domain with complete uv coverage, then Fourier transformed back to the image plane. The right panel shows the image convolved with a $0''.4$ FWHM Gaussian, the same as the super-resolved beam used in Fig. 2. The inclined torus model has successfully captured the aspect ratio of the overall structure, and has also reproduced the two lobe features, thus confirming that

they are due to projection of the optically thin equatorial belt.

A better way to compare between the model and data is to generate an image of the model with identical u - v sampling as the corresponding observation. Then the sampling effects will appear identically in both images, allowing a direct comparison. Fig. 7 & 8 show the images of the data compared to the best-fit models for selected epochs. The models were generated with the approach described above and then imaged using the same procedures as mentioned in §2. However, since the MEM algorithm is not applicable to images with negative values, we did not attempt to deconvolve the residual maps. We emphasize that the residual maps presented here only illustrate a qualitative comparison between the data and the model, rather than a detailed quantitative description of the underlying difference. The most obvious feature in the residuals is the flux deficit of the model torus in the southeast and northwest, and the excess emission at the center. The discrepancies are due to limitations of our relatively simple model. As indicated by the super-resolved images, the eastern lobe in the data is not reflection symmetric about its brightest point, but extends further to the south. This cannot be easily described by the model, which approximates the asymmetry by a linear gradient. Although less obvious, a similar case occurs for the western lobe as well. On the other hand, the excess flux at the center of the model torus is due to the abrupt cutoff of the high latitude emission in the model. Since the inclination angle ζ is fixed during the fit, the ellipticity depends solely on the opening angle θ . A large θ is required by the fit in order to match the overall geometry, hence resulting in excess emission filling the interior. In real life, the radio emissivity is likely to be latitude dependent and to decay smoothly at high latitude, providing a slightly different overall ellipticity. A more realistic model should incorporate all these effects to address the above discrepancies.

4.2. 18 GHz Observations

The best-fit model for the 18 GHz observation of 2003 July is shown in Fig. 9, with the data and model visibilities plotted in Fig. 10. The diffracted-limited images were deconvolved the CLEAN algorithm. Similar to Fig. 7 & 8, no deconvolution has been applied to the residual map in order to avoid running the algorithm into noise. As shown in Table 2, the best fits have small $\chi^2/\nu \approx 1$, which are due to large measurement uncertainties (see Fig. 10). The best-fit parameters are plotted by the open circles in Fig. 5. They are all consistent with the 9 GHz results, except that θ is slightly smaller at 18 GHz. While the discrepancy in θ seems to suggest a frequency-dependent emission height that implies different physical conditions between the equatorial plane and at higher latitude, it could also be the result of systematic errors in the fits which we do not fully understand. As the remnant is getting brighter, future

observations will help to investigate this problem. Following Manchester et al. (2005), slices through the 18 GHz diffraction-limited images along different P.A. were plotted in Fig. 11. In general, the two peaks in the model match well to the observation. The only exception is at 150° , where the data are $\sim 25\%$ brighter than the model in the east. As discussed in §4.1 above, this is attributed to the unmodeled southern extension of the lobe. The plot also illustrates the excess emission near the center of the model torus, again consistent with the 9 GHz results.

5. Discussion

5.1. Remnant Size

In general, the size of the torus is well-determined from the fits and is consistent with that determined in previous studies (Gaensler et al. 1997; Manchester et al. 2002; Gaensler et al. 2007). The best-fit radii from the torus and shell fits are comparable, but those from the shell plus two points model are always slightly larger. A similar discrepancy was also reported by Manchester et al. (2002), suggesting that the radius measurement is somewhat model-dependent. The average discrepancy is $\sim 5\%$ for the later epochs, which is attributed to the systematic errors in the modeling as mentioned in §3.2. In the following discussion, we assigned a 5% systematic errors for R . Hence the quadrature sum of these and the statistical errors obtained from bootstrapping provides the total uncertainties in R , which are shown by the dotted error flags in Fig. 5.

Compared to the measurements published for the X-ray shell (Park et al. 2007), the radio torus is larger by 10-15% which is too large to be accounted for by the measurement uncertainties. However, Gaensler et al. (2007) analysed the Chandra data in the Fourier domain and found that the X-ray and radio shells agree to better than 1% in size. Hence they argued that the discrepancy is due to different measuring techniques, rather than any physical difference. At optical wavelengths, Michael et al. (1998) reported that the reverse shock was located at 70% of the inner circumstellar ring around day 3900. This gives a radius of $0''.64$, which is slightly smaller than the torus size at that epoch. From the steady increase in the radio light curve, Manchester et al. (2005) argued that the radio-emitting electrons could be filling the region between the shocks. Although the thickness δ is not too sensitive in the fits and generally very small, this is still consistent with the prediction. With a density profile $\rho(r, t) \propto t^{-3}(r/t)^{-9}$ in the supernova ejecta (Eastman & Kirshner 1989), numerical simulations suggest that during the early stage of the SNR evolution, the forward and reverse shocks are separated only by 10-20% in radius (e.g., Truelove & McKee 1999). For SN 1993J, Bartel et al. (2007) reported a shell thickness of 30% of the inner shell

radius. Despite the above results assuming a spherical symmetry, if δ in our case is of a similar order, given that the whole remnant is barely resolved in the 9 GHz observations, δ likely remains unresolved. This also supports the conclusion of Gaensler et al. (2007) that both thick and thin shell models provide equally good fits to the data.

5.2. Rate of Expansion

At the earliest epoch, the remnant has a radius of about 0.6. As Gaensler et al. (1997) pointed out, this implies a minimum mean expansion rate of 30000 km s^{-1} during the period 1987 to 1992, in the free expansion phase. This expansion was then followed by a drastic deceleration to $\sim 3000 \text{ km s}^{-1}$ at around the time the radio emission re-emerged (Gaensler et al. 1997). To determine the expansion since day 1800, we employed a linear fit to R for all the 9 GHz observations and obtained an expansion velocity of $v = 4000 \pm 400 \text{ km s}^{-1}$ over the period 1992-2008. The small $\chi^2/\nu = 0.2$ in the fit indicates that the measurement uncertainties are over-estimated. On the other hand, if only the statistical errors are considered, the result is similar ($v = 4150 \pm 30 \text{ km s}^{-1}$), but with smaller errors and a much larger $\chi^2/\nu = 9.0$. Gaensler et al. (2007) performed a quadratic fit to the remnant size and suggested an acceleration in the expansion. We also found a similar trend in our results. However, a F -test suggests that the quadratic fit is not statistically significant: there is a 20% probability that the smaller χ^2 in the quadratic fit would occur solely by chance. Therefore, we conclude that the simpler model (i.e. linear fit) is preferred and adopt the linear expansion $v = 4000 \pm 400 \text{ km s}^{-1}$ in the following discussion. This value lies between $v = 4700 \pm 100 \text{ km s}^{-1}$ and $\sim 3700 \text{ km s}^{-1}$ obtained by Gaensler et al. (2007) and Manchester et al. (2002) respectively using a thin shell model, and agrees with the prediction $v = 4100 \text{ km s}^{-1}$ from hydrodynamic simulations (Borkowski et al. 1997). It is also similar to the expansion rate of the reverse shock at $v = 3700 \pm 900 \text{ km s}^{-1}$ reported by Michael et al. (1998). On the other hand, the X-ray expansion is apparently much faster before day 6200. Early measurements showed an X-ray expansion of $v = 4200 \text{ km s}^{-1}$ (Park et al. 2004), but Park et al. (2007) recently suggested acceleration to a higher velocity of $v \sim 6000 \text{ km s}^{-1}$ over the period covering 5000-6000, before the expansion decelerates to $v = 1400 \text{ km s}^{-1}$ near day 6200. This could indicate that the X-ray emission is located differently as the radio emission and much closer to the forward shock.

A comparison between the radio and optical observations suggests that the supernova blast wave may have started to encounter the dense CSM in the past few years. The optical ring, the emission from which represents fluorescence after ionization of the CSM by the supernova UV flash, indicates the inner boundary of the dense swept-up CSM. As seen

by the *HST*, the central equatorial ring has a radius of $0''.81$ - $0''.85$ (Burrows et al. 1995; Plait et al. 1995). Accounting for the uncertainties in both the radio and optical measurements, our results suggest that the radio emission could have reached the optical inner ring around day 6000-6500, hence the forward shock could have started to expand into the dense CSM as early as 2004. This falls nicely within the predictions by Chevalier & Dwarkadas (1995), Gaensler et al. (1997) and Manchester et al. (2002), but disagrees with other estimates such as those of Luo et al. (1994) and Borkowski et al. (1997). The X-ray observations also provide evidence for the encounter. The rapid increase in the soft X-ray flux near day 6000-6200 (Park et al. 2005) and the drastic deceleration of the X-ray expansion around day 6200 (Park et al. 2007) reveal that the forward shock has encountered a steep gradient in the ambient density. We expect a similar deceleration in the radio expansion to occur very soon.

5.3. Emission Height

In addition to the radius, the opening angle θ is also an important parameter that probes the CSM geometry. The best-fit values of θ shown in Fig. 5 are substantial, indicating a significant level of radio emission from mid-latitudes. This extra-planar structure implies the spread of dense CSM over large regions on either side of the equatorial plane, and suggests that the prominent optical ring is merely the densest part of a more complicated 3D structure. In the later epochs, θ stays nearly constant around 40° . This gives an inferred emission height up to $\sim 5 \times 10^{17}$ cm from the equatorial plane. Our result indicates a radio emission geometry very similar to that of the reverse shock. Michael et al. (1998, 2003) reported a rapid decrease of $\text{Ly}\alpha$ and $\text{H}\alpha$ emission beyond 40° and hence deduced that the reverse shock is mostly confined within 30° of the equatorial plane. Our fitting results also provide the characteristic structure of the CSM, which can be compared to hydrodynamic simulations such as those of Blondin & Lundqvist (1993), Martin & Arnett (1995) and Morris & Podsiadlowski (2007). In those simulations, the exact shape of the contact discontinuity between the BSG and RSG winds is highly model-dependent. Some models suggest a rather constant opening angle over a large range of radius (e.g. Fig. 3 of Martin & Arnett 1995), which is similar to our case. Nevertheless, all the simulations indicate that the overall geometry of the swept-up CSM is peanut-like, with a dense equatorial ring at the waist. This picture predicts that the radio emission will extend with time to higher latitude. Although the expected trend is not found in the current data, we anticipate θ to increase significantly in future observations according to the above models. Eventually the shock will reach the dense CSM in the polar region and the radio morphology will be more circular. Our results do not show any polar protrusions as suggested by Blondin et al. (1996). If the forward shock continues to expand at a similar

rate, it may take another 10-20 years to reach the polar region before we can verify these predictions. As a note, Fig. 5 suggests some hints that θ is slightly larger in the early epochs. If this is real, it may indicate the encounter of ejecta with dense regions at higher latitude at the early stages. Along with the shock expansion, the radio emission is then gradually dominated by other regions closer to the equatorial plane, resulting in a gradual decrease in θ .

5.4. Asymmetry

The super-resolved images in Fig. 2 clearly show that the eastern lobe is brighter than its western counterpart. This feature has also been reported in the X-ray observations (Burrows et al. 2000; Park et al. 2002; Michael et al. 2002). In our torus model, the asymmetry is quantified in terms of a linear gradient with direction ϕ and magnitude g . Fig. 5 shows a trend of increase in ϕ prior to 1998. Although this occurred at a similar time as the optical hot spots first appeared, comparing ϕ to the hot spot positions shows that they do not coincide. Therefore we arrive the same conclusion as Manchester et al. (2002) that the detailed morphology of radio and optical emissions are not correlated. The only similarity is that they both brightened first in the eastern half, indicating a global asymmetry along the east-west direction. On the other hand, the variation in ϕ may be associated with the slight decrease in θ around that period. This could suggest that the blast wave has encountered different dense regions before and after ~ 1998 . In the late epochs, ϕ stays around 110° , which corresponds to a P.A. of 96° on the plane of the sky. This matches the bright X-ray lobes located at P.A. 90° and 270° as reported by Park et al. (2002).

Although there were indications from earlier data that the asymmetry increases with time (Gaensler et al. 1997; Manchester et al. 2002), the longer data span presented here does not support this. From 1995 onward, g stays at a constant level of $\sim 40\%$. This gives a flux ratio of 1.5 between the two halves of the torus at the equatorial plane. The projection onto the plane of the sky reduces this ratio slightly. Thus as seen by an observer, the eastern lobe appears to be ~ 1.4 times brighter than the west. In order to confirm this result, we compared to the degree of asymmetry inferred from the shell plus two points fits. The surface brightness ratio between the eastern and western lobes is listed in Table 3; again this does not show any significant long-term variations, but suggests a rather constant flux ratio of about 1.3, which is consistent with the torus estimate. Hence we conclude that the surface brightness of the eastern half is consistently 30-40% larger than the west. This is very close to the 40% asymmetry in the reverse shock (Michael et al. 2003), also similar to the 15-50% asymmetry in the 0.3-6 keV X-ray band (Michael et al. 2002). While the exact origin of the

east-west asymmetry still remains unclear, it seems likely that the asymmetry either lies in the initial velocity of the ejecta, which would imply an asymmetric explosion, or in the density of the CSM (Gaensler et al. 1997; Sugerman et al. 2002). In principle the evolution of the radio morphology can help distinguish these two scenarios. If the eastern lobe expands faster, it will cause a systematic shift of the torus center towards the east. Unfortunately, the phase self-calibration process removes the absolute astrometric information in the data, precluding a direct comparison between epochs. Nonetheless, the shell plus two points fit can provide some insights into the relative positions of the features. Although this model is less preferable than the torus model, both of them obtain a comparable goodness-of-fit, therefore we believe that the former can still provide a sensible description of the location of the lobe centroids. As listed in Table 3, the offsets of the point sources from the shell center increase at a similar rate as the shell radius. This would not be the case if the CSM were denser towards the east, since the higher density would lead to a larger deceleration for the eastern lobe. In the other scenario, if the ejecta in the east had a higher velocity, then it would arrive at the equatorial ring first and would start to decelerate. Hence we expect the ratio of offsets to vary in future observations. However, we emphasize that this is only a very rough estimate. In particular, if the shell plus two points model is not a good description of the physical structure, excess flux from the lobes will shift the center of the underlying shell, introducing large systematic errors in the positions.

5.5. Limit on Radio Flux of a Central Source

In spite of extensive searches in radio and optical wavelengths, no pulsar has yet been found within the supernova remnant (Manchester 2007). Our fitting scheme can also provide a detection limit on any possible central object. We applied the same fitting procedure using the torus model with a point source fixed at the center. The flux density of the point source was held fixed during the fit. We adjusted its level until the change in the best-fit χ^2 value exceeded a certain limit. To begin with, we applied the fit to the 1996 July observation, in which the remnant has high S/N but is still not too bright to preclude a sensitive search. The fit gives a 3σ upper limit of 0.3 mJy. Applying the fit on several other epochs obtained very similar results. Hence we conclude that this is the 3σ detection limit on any unresolved central source, including a neutron star or a compact pulsar wind nebula, for the ATCA observations at 9 GHz. As a comparison, the most sensitive limit on pulsation at this frequency yields an upper flux limit of 0.058 mJy (Manchester 2007).

5.6. Comparison to Other Radio Supernova Remnants

Among about ten resolved radio supernovae (RSNe) (see Bietenholz 2005), SN 1987A shows a very different characteristics in the asymmetry, morphology and expansion as compared to the others. For example, SN 1993J in M81, which is the best studied RSN besides SN 1987A, was found to be circular within 3% over 7 years of VLBI observations. Based on a statistical argument, Bietenholz et al. (2003) suggested that the emission is intrinsically spherical. On the other hand, only two other RSNe show large deviation from a circular shell. VLBI imaging of SN 1986J in NGC 891 revealed a distorted shell structure with a hot spot (Bietenholz et al. 2004). Pérez-Torres et al. (2002) suggested this could be due to protrusions in the progenitor’s wind (Blondin et al. 1996), or jet-induced core collapse (Khokhlov et al. 1999). Another example of a non-spherical RSN is SN 2004et in NGC 6946. A recent study by Martí-Vidal et al. (2007) interpreted the asymmetry as either a shell with two hot spots, which could be similar to the case of SN 1987A, or an anisotropically expanding shell with a protrusion.

The main distinction between SN 1987A and other RSNe lies in its rate of expansion. As discussed, the expansion of SN 1987A must have undergone a rapid deceleration in the first 1800 days. In contrast, for all other RSNe with detected expansion, their sizes are well-approximated by a power-law $R \propto t^m$, with the deceleration parameter $m \sim 0.7 - 1$ (Bietenholz 2005). The most extreme example is SN 1979C in M100, which has shown nearly free expansion ($m \approx 1$) for over 22 years (Bartel & Bietenholz 2003). The unusual morphology and evolution of SN 1987A can be largely attributed to its complex circumstellar environment. Thus, this extraordinary event provides a unique example in the study of supernova shell dynamics, stellar wind interactions and stellar evolution.

6. Conclusions

In this study, we have developed a scheme to model the interferometric $u-v$ data for any 3D object with axisymmetric structure. An application to ATCA 9 and 18 GHz observations of SN 1987A has improved the spatial modeling of the radio remnant. An inclined equatorial belt torus model in 3D was employed, with the incorporation of light travel time effects and of an overall east-west asymmetry. The projected brightness distribution of the model is transformed into 2D Fourier space analytically, then is fit directly to the visibility data. The torus model successfully captures the characteristic features of the radio morphology and provides substantial improvements over the simple spherical shell fit used in previous studies. The best-fit torus geometry shows significant extra-planar emission extending to mid-latitudes $\sim 40^\circ$, and a 40% flux difference between the eastern and western lobes.

Evolution of the shell radius with time implies a constant expansion rate of $4000 \pm 400 \text{ km s}^{-1}$ over the period 1992-2008 covered by the observations; the radio remnant is probably now starting to encounter the optical inner ring. Our results suggest a torus geometry and expansion speed both very similar to those seen in $\text{H}\alpha$ and $\text{Ly}\alpha$ emission, indicating that the radio synchrotron emission originates between the supernova forward and reverse shocks. In summary, the torus fitting provides a powerful tool to probe the 3D structure of the radio emission, showing that the overall picture of the dense CSM is consistent with the hydrodynamic simulation of the progenitor star's interacting winds. Future evolution of the radio morphology can help differentiate between specific evolutionary histories for this system, and can address the apparent east-west asymmetry in the ejecta distribution.

Facilities: ATCA ()

We thank Shami Chatterjee for useful discussions. The Australia Telescope is funded by the Commonwealth of Australia for operation as a National Facility managed by CSIRO. B.M.G. and R.N.M. acknowledge the support of the Australian Research Council.

REFERENCES

- Ball, L., Crawford, D. F., Hunstead, R. W., Klamer, I., & McIntyre, V. J. 2001, *ApJ*, 549, 599
- Ball, L., & Kirk, J. G. 1992, *ApJ*, 396, L39
- Bartel, N., & Bietenholz, M. F. 2003, *ApJ*, 591, 301
- Bartel, N., Bietenholz, M. F., Rupen, M. P., & Dwarkadas, V. V. 2007, *ApJ*, 668, 924
- Bietenholz, M. 2005, in *ASP Conf. Ser. 340, Future Directions in High Resolution Astronomy: The 10th Anniversary of the VLBA*, ed. J. Romney & M. Reid (San Francisco: ASP), 286
- Bietenholz, M. F., Bartel, N., & Rupen, M. P. 2003, *ApJ*, 597, 374
- Bietenholz, M. F., Bartel, N., & Rupen, M. P. 2004, *Science*, 304, 1947
- Blondin, J. M., Lundqvist, P. & Chevalier, R. A. 1993, *ApJ*, 472, 257
- Blondin, J. M., & Lundqvist, P. 1993, *ApJ*, 405, 337
- Borkowski, K. J., Blondin, J. M., & McCray, R. 1997, *ApJ*, 476, L31

- Bracewell, R. N. 2000, *The Fourier Transform and Its Applications* (Boston: McGraw Hill)
- Bridle, A. H., & Schwab, F. R. 1999, in *ASP Conf. Ser. 180, Synthesis Imaging in Radio Astronomy II*, ed. G. B. Taylor, C. L. Carilli, & R. A. Perley (San Francisco: ASP), 371
- Briggs, D. S. 1994, in *The Restoration of HST Images and Spectra - II*, ed. R.J. Hanisch & R.L. White (Baltimore: STScI), 250
- Burrows, C. J., et al. 1995, *ApJ*, 452, 680
- Burrows, D. N., et al. 2000, *ApJ*, 543, L149
- Chevalier, R. A., & Dwarkadas, V. V. 1995, *ApJ*, 452, L45
- Collins, T. J. B., Frank, A., Bjorkman, J. E., & Livio, M. 1999, *ApJ*, 512, 322
- Crotts, A. P. S., & Heathcote, S. R. 1991, *Nature*, 350, 683
- Duffy, P., Ball, L., & Kirk, J. G. 1995, *ApJ*, 447, 364
- Eastman, R. G., & Kirshner, R. P. 1989, *ApJ*, 347, 771
- Efron, B., & Tibshirani, R. J. 1993, *An Introduction to the Bootstrap* (New York: Chapman and Hall)
- Ekers, R. D. 1999, in *ASP Conf. Ser. 180, Synthesis Imaging in Radio Astronomy II*, ed. G. B. Taylor, C. L. Carilli, & R. A. Perley (San Francisco: ASP), 321
- Frater, R. H., Brooks, J. W., & Whiteoak, J. B. 1992, *Journal of Electrical and Electronics Engineering Australia*, 12, 103
- Gaensler, B. M., Manchester, R. N., Staveley-Smith, L., Tzioumis, A. K., Reynolds, J. E., Kesteven, M. J. 1997, *ApJ*, 479, 845
- Gaensler, B. M., Staveley-Smith, L., Manchester, R. N., Kesteven, M. J., Ball, L., & Tzioumis, A. K. 2007, in *AIP Conf. Proc. 937, Supernova 1987A: 20 Years After: Supernovae and Gamma-Ray Bursters*, ed. S. Immler, K.W. Weiler, & R. McCray, (New York: AIP), 86
- Gull, S. F., & Daniell, G. J. 1978, *Nature*, 272, 686
- Jun, B.-I., & Norman, M. L. 1996, *ApJ*, 465, 800

- Khokhlov, A. M., Höflich, P. A., Oran, E. S., Wheeler, J. C., Wang, L., & Chtchelkanova, A. Y. 1999, *ApJ*, 524, L107
- Kwok, S. 1982, *ApJ*, 258, 280
- Luo, D., McCray, R., & Slavin, J. 1994, *ApJ*, 430, 264
- Manchester, R. N. 2007, in *AIP Conf. Proc. 937, Supernova 1987A: 20 Years After: Supernovae and Gamma-Ray Bursters*, ed. S. Immler, K.W. Weiler, & R. McCray, (New York: AIP), 134
- Manchester, R. N., Gaensler, B. M., Wheaton, V. C., Staveley-Smith, L., Tzioumis, A. K., Bizunok, N. S., Kesteven, M. J., & Reynolds, J. E. 2002, *PASA*, 19, 207
- Manchester, R. N., Gaensler, B. M., Staveley-Smith, L., Kesteven, M. J., & Tzioumis, A. K. 2005, *ApJ*, 628, L131
- Martin, C. L., & Arnett, D. 1995, *ApJ*, 447, 378
- Martí-Vidal, I., et al. 2007, *A&A*, 470, 1071
- Michael, E., et al. 1998, *ApJ*, 509, L117
- Michael, E., et al. 2002, *ApJ*, 574, 166
- Michael, E., et al. 2003, *ApJ*, 593, 809
- Morris, T., & Podsiadlowski, P. 2007, *Science*, 315, 1103
- Ng, C.-Y., & Romani, R. W. 2008, *ApJ*, 673, 411
- Park, S., Burrows, D. N., Garmire, G. P., Nousek, J. A., McCray, R., Michael, E., & Zhekov, S. 2002, *ApJ*, 567, 314
- Park, S., Zhekov, S. A., Burrows, D. N., Garmire, G. P., & McCray, R. 2004, *ApJ*, 610, 275
- Park, S., Zhekov, S. A., Burrows, D. N., & McCray, R. 2005, *ApJ*, 634, L73
- Park, S., Burrows, D. N., Garmire, G. P., McCray, R., Racusin, J. L., & Zhekov, S. A. 2007, in *AIP Conf. Proc. 937, Supernova 1987A: 20 Years After: Supernovae and Gamma-Ray Bursters*, ed. S. Immler, K.W. Weiler, & R. McCray, (New York: AIP), 43
- Pérez-Torres, M. A., Alberdi, A., Marcaide, J. M., Guirado, J. C., Lara, L., Mantovani, F., Ros, E., & Weiler, K. W. 2002, *MNRAS*, 335, L23

- Plait, P. C., Lundqvist, P., Chevalier, R. A., & Kirshner, R. P. 1995, *ApJ*, 439, 730
- Press, W. H., Flannery, B. P., Teukolsky, S., & Vetterling, W. 1992, *Numerical Recipes in C: The Art of Scientific Computing* (Cambridge: Cambridge Univ. Press), 691
- Pun, C. S. J. 2007, in *AIP Conf. Proc.* 937, *Supernova 1987A: 20 Years After: Supernovae and Gamma-Ray Bursters*, ed. S. Immler, K.W. Weiler, & R. McCray, (New York: AIP), 171
- Pun, C. S. J., et al. 2002, *ApJ*, 572, 906
- Sault, R. J., Teuben, P. J., & Wright, M. C. H. 1995, in *ASP Conf. Ser.* 77, *Astronomical Data Analysis Software and Systems IV*, ed. R. Shaw, H. E. Payne, & J. J. E. Hayes (San Francisco: ASP), 433
- Staveley-Smith, L., et al. 1992, *Nature*, 355, 147
- Staveley-Smith, L., Briggs, D. S., Rowe, A. C. H., Manchester, R. N., Reynolds, J. E., Tzioumis, A. K., & Kesteven, M. J. 1993a, *Nature*, 366, 136
- Staveley-Smith, L., Manchester, R. N., Kesteven, M. J., Tzioumis, A. K., & Reynolds, J. E. 1993b, *PASA*, 10, 331
- Staveley-Smith, L., Gaensler, B. M., Manchester, R. N., Ball, L., Kesteven, M. J., & Tzioumis, A. K. 2007, in *AIP Conf. Proc.* 937, *Supernova 1987A: 20 Years After: Supernovae and Gamma-Ray Bursters*, ed. S. Immler, K.W. Weiler, & R. McCray, (New York: AIP), 96
- Sugerman, B. E. K., Lawrence, S. S., Crofts, A. P. S., Bouchet, P., & Heathcote, S. R. 2002, *ApJ*, 572, 209
- Sugerman, B. E. K., Crofts, A. P. S., Kunkel, W. E., Heathcote, S. R., & Lawrence, S. S. 2005a, *ApJ*, 627, 888
- Sugerman, B. E. K., Crofts, A. P. S., Kunkel, W. E., Heathcote, S. R., & Lawrence, S. S. 2005b, *ApJS*, 159, 60
- Truelove, J. K., & McKee, C. F. 1999, *ApJS*, 120, 299
- Turtle, A. J., Campbell-Wilson, D., Bunton, J. D., Jauncey, D. L., & Kesteven, M. J. 1987, *Nature*, 327, 38
- Turtle, A. J., Campbell-Wilson, D., Manchester, R. N., Staveley-Smith, L., & Kesteven, M. J. 1990, *IAU Circ.* 5086

A. Two Dimensional Fourier Transform of an Inclined Torus Model

In this section, we give a mathematical description of an inclined torus model and derive an analytic expression for its Fourier transform. Although a specific example of a torus model is considered here, the expression could be easily generalized to any objects with axisymmetry.

We first set up a coordinate system (x', y', z') with z' along the symmetric axis and y' along the projected line of sight at the equatorial plane. In this frame, a model torus (or any axisymmetric object) can be built up from rings centered at $(0, z')$ with radius r

$$I^{\text{torus}}(x', y') = \iint w I_{r, z'}^{\text{ring}} dr dz' ,$$

where the intensity of each ring is given by $I_{r, z'}^{\text{ring}} = f \delta \left(r - \sqrt{x'^2 + y'^2} \right)$. In our case, the weight factor has value $w \equiv 1$ as the torus has a uniform emissivity. Applying the Hankel Transform (Bracewell 2000), each ring in the Fourier domain is given by

$$F^{\text{ring}}(u, v) \equiv \mathcal{F}\{I^{\text{ring}}\} = J_0 \left(2\pi r \sqrt{u^2 + v^2} \right)$$

where J_0 is the Bessel Function of the First Kind. In order to account for the asymmetry observed in the remnant, we assume that the flux density of the torus varies linearly at a rate g along the direction ϕ in the equatorial plane (see Fig. 3). Hence the intensity of each ring is modified to

$$I^{\text{asym}} = [g(x' \cos \phi + y' \sin \phi) + 1] I^{\text{ring}} .$$

With the Convolution Theorem (Bracewell 2000), the Fourier transform of an asymmetric ring is then

$$\begin{aligned} F^{\text{asym}}(u, v) &\equiv \mathcal{F}\{I^{\text{asym}}\} \\ &= \mathcal{F}\{g(x' \cos \phi + y' \sin \phi) + 1\} * \mathcal{F}\{I^{\text{ring}}\} \\ &= \left\{ \frac{ig}{2\pi} [\cos \phi \delta'(u) \delta(v) + \sin \phi \delta(u) \delta'(v)] + \delta(u) \delta(v) \right\} * F^{\text{ring}}(u, v) \\ &= \left[\frac{ig}{2\pi} \left(\cos \phi \frac{\partial}{\partial u} + \sin \phi \frac{\partial}{\partial v} \right) + 1 \right] F^{\text{ring}}(u, v) \\ &= -\frac{irg}{\sqrt{u^2 + v^2}} (u \sin \phi + v \cos \phi) J_1 \left(2\pi r \sqrt{u^2 + v^2} \right) + J_0 \left(2\pi r \sqrt{u^2 + v^2} \right) , \end{aligned}$$

where $**$ denotes a 2D convolution such that

$$F ** G \equiv \int_{-\infty}^{+\infty} \int_{-\infty}^{+\infty} F(u, v) G(u - u', v - v') du' dv'$$

for any 2D functions $F(u, v)$ and $G(u, v)$. $\delta(u), \delta(v)$ are Dirac's δ functions and $\delta'(u) \equiv \frac{d\delta}{du}$ and $\delta'(v) \equiv \frac{d\delta}{dv}$.

The model torus has to be projected onto the plane of the sky before it is compared to the observations. Here we set up another coordinate system (x, y, z) , with z along the observer line of sight and y along the projected torus axis on the image plane. The transformation between the two frames is given by

$$\begin{cases} x &= x' \\ y &= y' \sin \zeta - z' \cos \zeta \\ z &= y' \cos \zeta + z' \sin \zeta, \end{cases}$$

where ζ is the inclination angle between the torus equatorial plane and the observer line of sight (see Fig. 3). The projection essentially compresses the rings into ellipses in the image plane, with center at $(x, y) = (0, -z' \cos \zeta)$ and semi-minor axis $r \sin \zeta$. Hence an asymmetric ring projected on the image plane can be expressed as

$$I_{r,z'}^{\text{proj}}(x, y) = \left[g \left(x \cos \phi + \frac{y+z' \cos \zeta}{r \sin \zeta} \sin \phi \right) + 1 \right] f \delta \left(r - \sqrt{x^2 + \left(\frac{y+z' \cos \zeta}{\sin \zeta} \right)^2} \right).$$

Following the scaling and shifting properties of the Fourier Transform (Bracewell 2000), for any constants a and b ,

$$\begin{aligned} \mathcal{F}\{f(x - a, y - b)\} &= e^{-i2\pi(au+bv)} \mathcal{F}\{f\}(u, v) \\ \mathcal{F}\{f(ax, by)\} &= \frac{1}{|ab|} \mathcal{F}\{f\} \left(\frac{u}{a}, \frac{v}{b} \right), \end{aligned}$$

hence

$$F^{\text{proj}}(u, v) \equiv \mathcal{F}\{I^{\text{proj}}\} = e^{i2\pi z' v \cos \zeta} F^{\text{asym}}(u, v \sin \zeta)$$

up to an overall normalization factor.

To correct for light travel time effects, we assume the torus flux density f increases linearly during the light travel time across the remnant, i.e. $f \approx \dot{f}t + f_0$, for constants \dot{f} and f_0 . While the latter is a fitting parameter, the former is determined from the local derivative of the light curve given by Staveley-Smith et al. (2007). The relative light traveling time from each point of the ring to the observer is

$$\Delta t = \frac{z}{c} = \frac{d}{c} (y' \cos \zeta + z' \sin \zeta) = \frac{d}{c} \left(\frac{y}{\tan \zeta} + \frac{z'}{\sin \zeta} \right),$$

where $d = 51$ kpc is the distance to LMC, and z is in the units of radians. Hence the flux density at each point is

$$f = \frac{d\dot{f}}{c} \left(\frac{y}{\tan \zeta} + \frac{z'}{\sin \zeta} \right) + f_0$$

and the torus intensity is modified by a linear gradient of

$$\frac{d\dot{f}}{c f} \left(\frac{y}{\tan \zeta} + \frac{z'}{\sin \zeta} \right) + 1 .$$

Employing the Convolution Theorem again, we obtain the Fourier transform of an asymmetric ring including a light travel time correction

$$F^{\text{light}}(u, v) = \left[\frac{d\dot{f}}{c f} \left(\frac{i}{2\pi} \frac{1}{\tan \zeta} \frac{\partial}{\partial v} + \frac{z'}{\sin \zeta} \right) + 1 \right] F^{\text{proj}}(u, v) .$$

Finally, the model is shifted and rotated according to (x_0, y_0) and Ψ respectively,

$$F^{\text{final}}(u, v) = e^{-i2\pi(x_0u+y_0v)} F^{\text{light}}(u \cos \Psi - v \sin \Psi, u \sin \Psi + v \cos \Psi)$$

and integrated through r and z' since the Fourier transform is linear.

$$F^{\text{torus}}(u, v) = \iint w F_{r,z'}^{\text{final}} dr dz' .$$

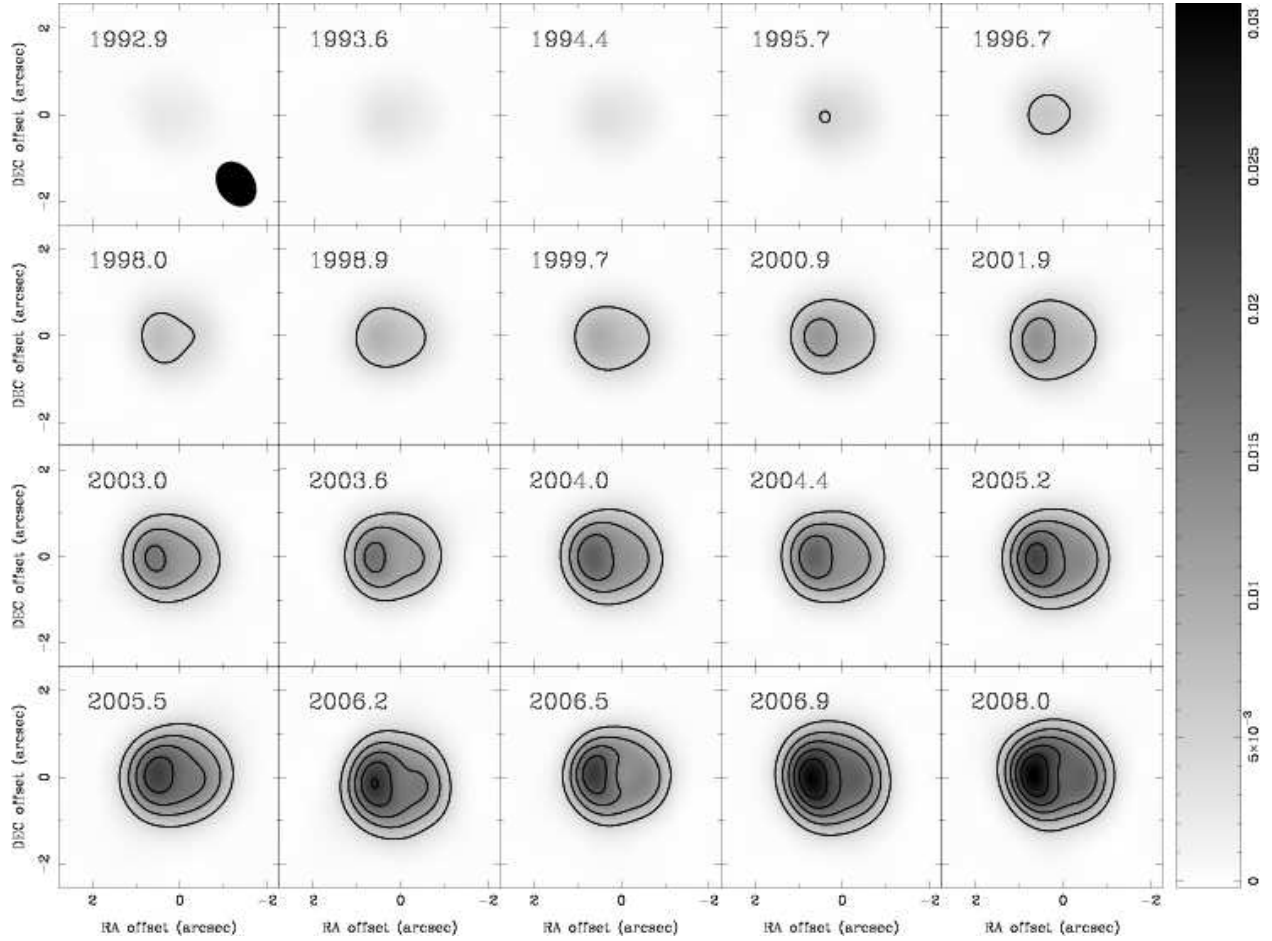


Fig. 1.— Diffraction-limited 9 GHz ATCA images of SN 1987A over the period 1992 to 2008. Some epochs have been averaged together to boost the S/N (see Table 1). The scale is linear, ranging from -0.2 to 31 mJy beam^{-1} . The contours are at levels from 5 to 30 mJy beam^{-1} with 5 mJy beam^{-1} intervals. The synthesized beam for the first epoch is shown in the first panel as an ellipse. The beams for the other epochs vary slightly in orientation, but are similar in size.

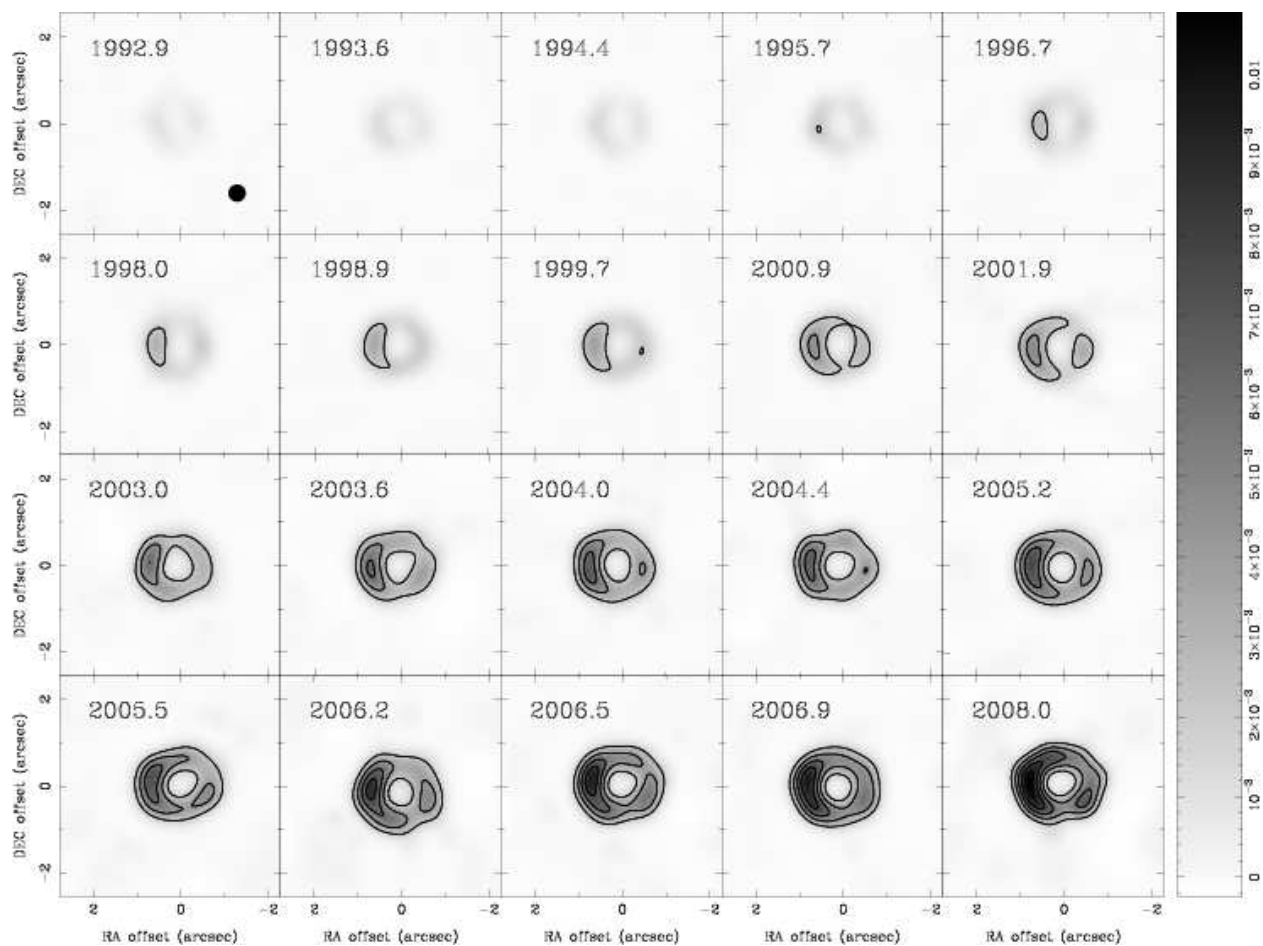


Fig. 2.— Super-resolved 9 GHz ATCA images of SN 1987A over the period 1992 to 2008. Similar to Fig. 1, some epochs have been averaged to boost the S/N (see Table 1). The scale is linear, ranging from -0.2 to $10.8 \text{ mJy beam}^{-1}$. The contours are at levels from 2 to 10 mJy beam^{-1} with 2 mJy beam^{-1} intervals. The synthesized beam, which is shown in the first panel, is a circular Gaussian with FWHM $0''.4$.

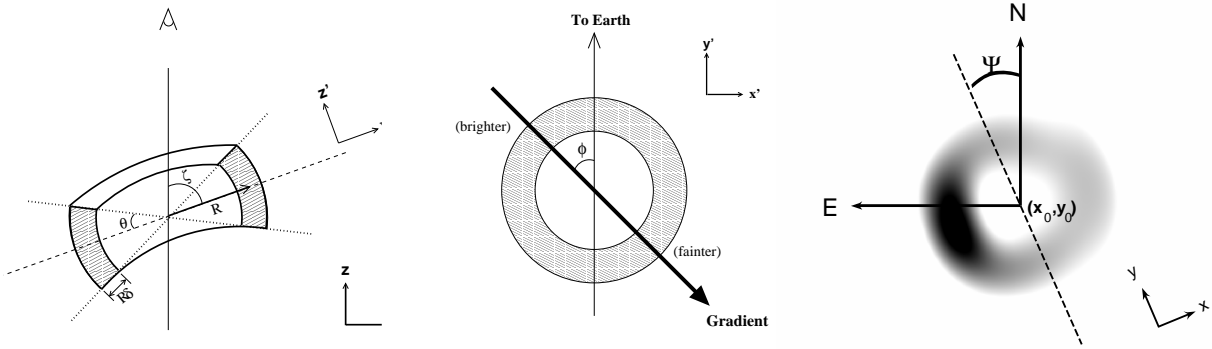


Fig. 3.— Schematic diagrams illustrating the geometric parameters in the torus model. *Left:* cross-section of the torus model, as viewed perpendicular to the observer line of sight. *Middle:* the torus in the equatorial plane showing a linear gradient, defined from the brighter side toward the fainter side. *Right:* A model torus, which is generated with parameters similar to that of the best-fit model for the most recent epoch (2008.0), projected onto the image plane (i.e. the plane of the sky).

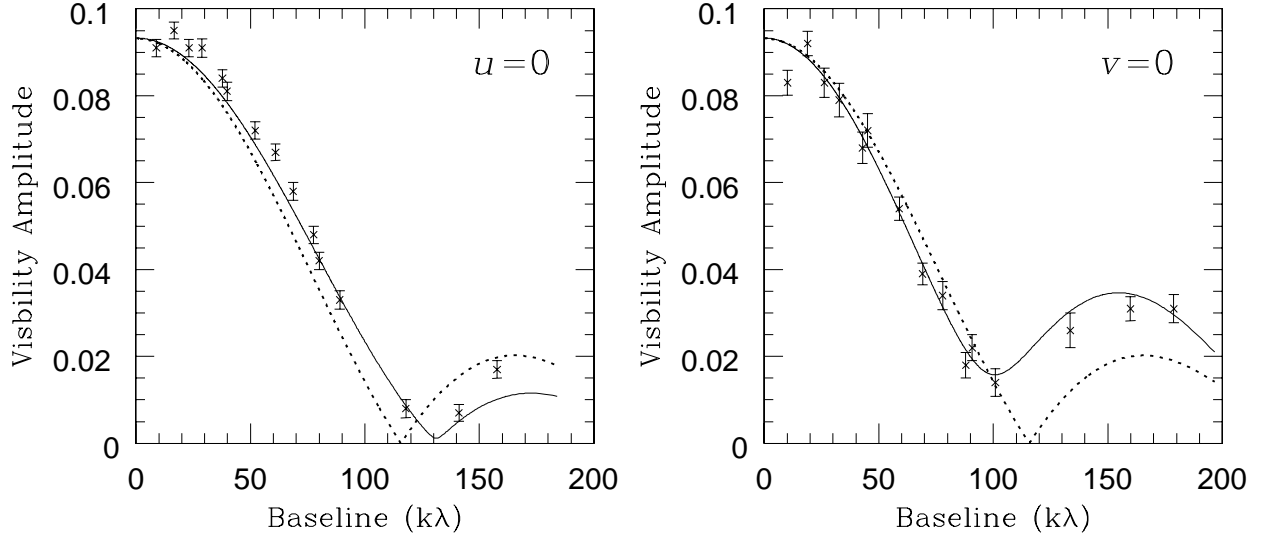


Fig. 4.— Amplitude of the visibility data in the most recent epoch (2008.0) of ATCA 9 GHz data compared to the best-fit torus and thin spherical shell models. The torus and shell models are plotted by the solid and dotted lines respectively. The two panels show slices through the u - v domain along the axes $u = 0$ and $v = 0$.

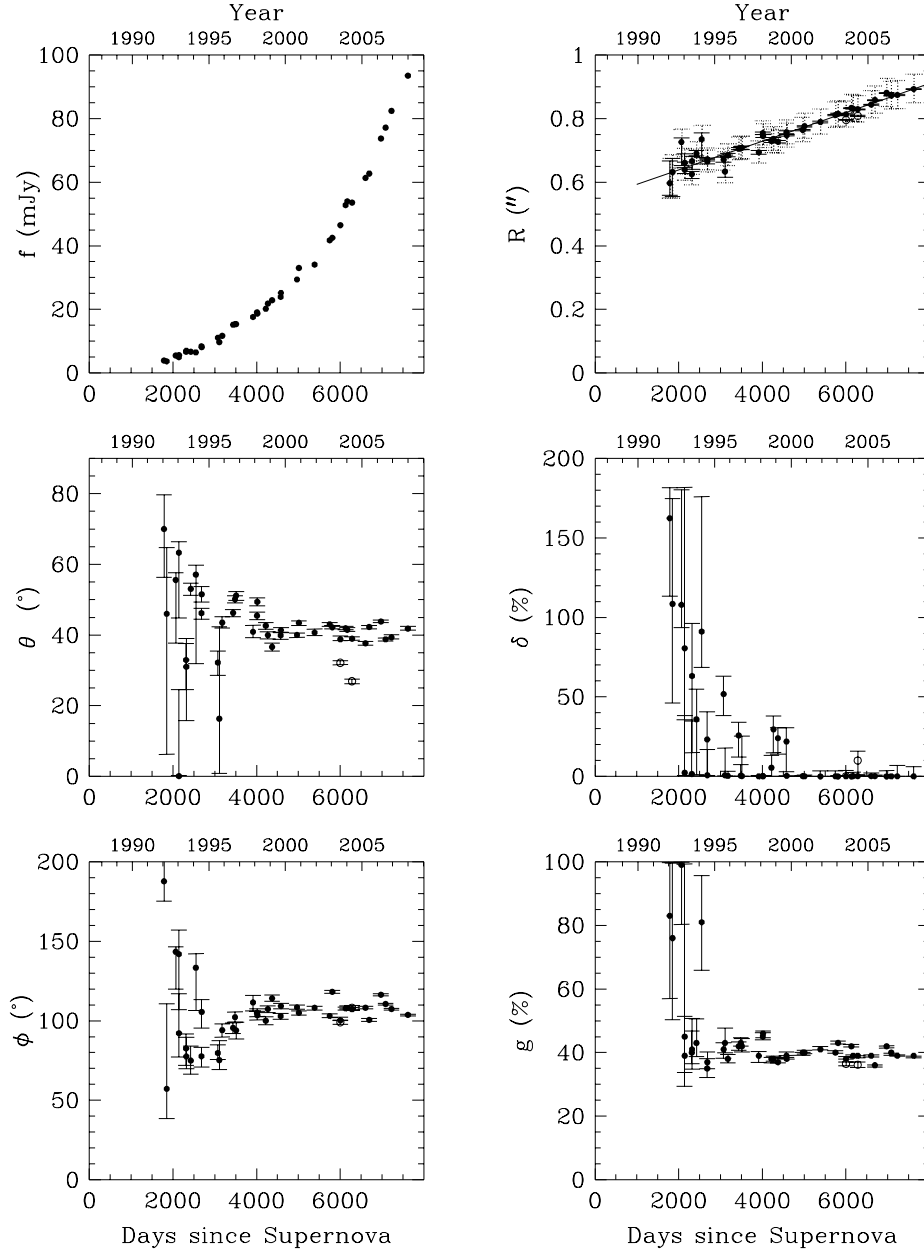


Fig. 5.— The best-fit flux density (f), radius (R), opening angle (θ), shock thickness (δ), gradient angle (ϕ) and gradient magnitude (g) at each epoch, obtained from the equatorial belt torus model as described in §3.1. The results for the 9 and 18 GHz observations are plotted as filled and open circles respectively. Note that we did not plot the flux density for the 18 GHz observations, since the absolute flux scale has not been fully calibrated. The uncertainties in flux density is negligible. The dotted error flags in R indicate the total uncertainties, which are the quadrature sum of the statistical and systematic errors. The best-fit linear expansion in radius of 4000 km s^{-1} is shown by the straight line.

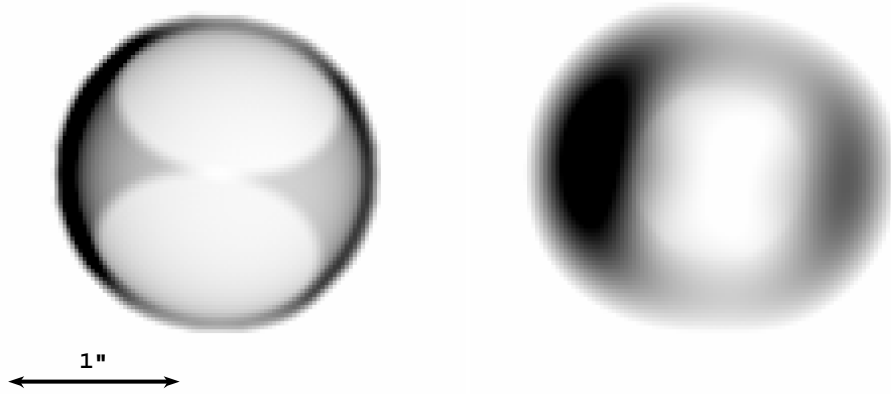


Fig. 6.— *Left:* The best-fit model for the most recent epoch (2008.0), with the parameters listed in Table 2. *Right:* The same model convolved with a $0''.4$ FWHM Gaussian kernel, as the super-resolved beam used in Fig. 2. The brightness scales in these images are arbitrary.

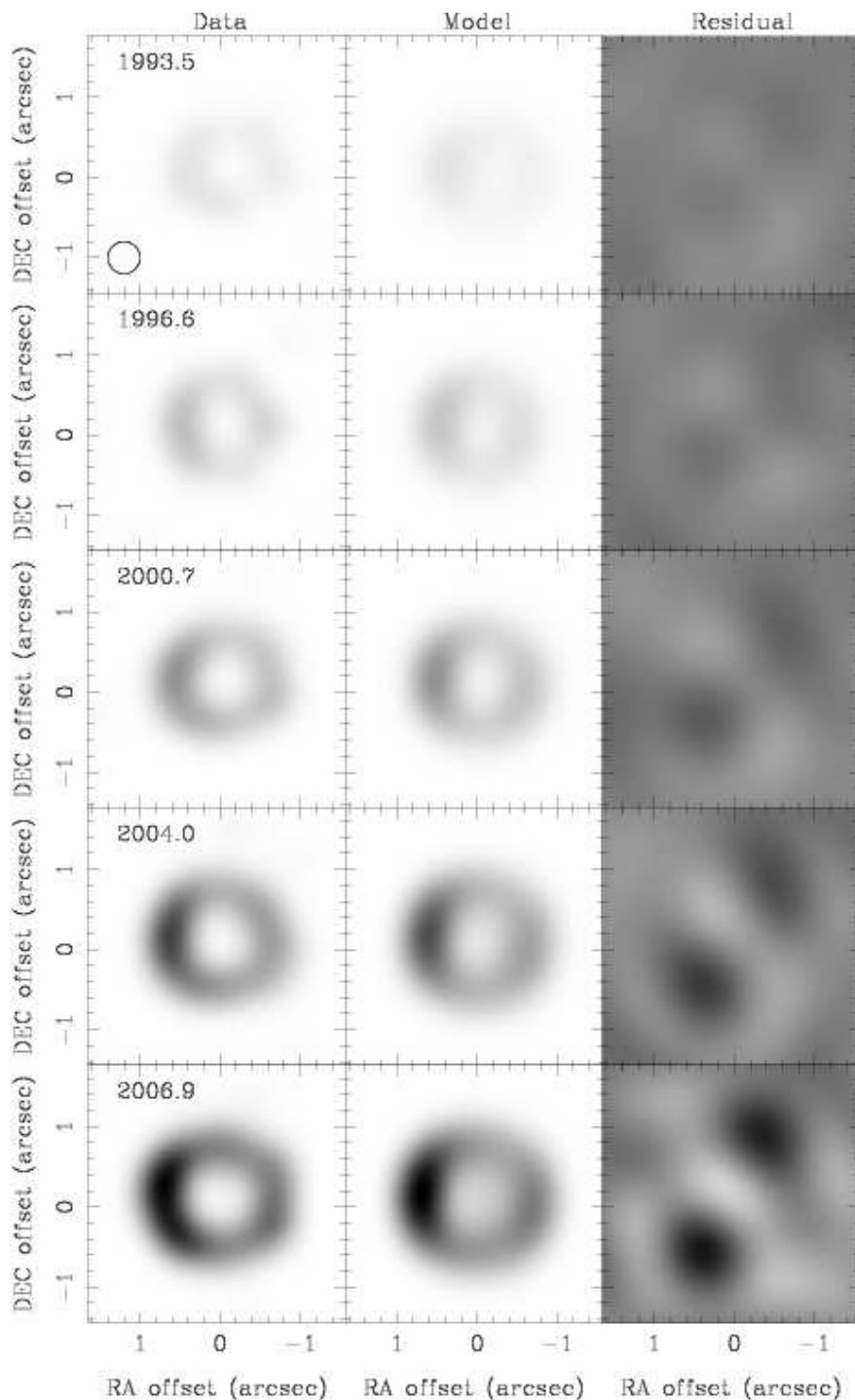


Fig. 7.— Super-resolved images at 9 GHz (*left column*) compared to the best-fit models (*middle column*) for selected epochs. These images were generated with the same procedure described in §3. The synthesized beam, which is a circular Gaussian with FWHM $0''.4$, is shown in the first panel. The right column shows the dirty maps of the residual visibilities, for which no deconvolution has been applied. The scales are linear, ranging from 0 to 10 mJy beam⁻¹ in the left and middle panels and from -1.5 to 1.5 mJy beam⁻¹ for the residuals.

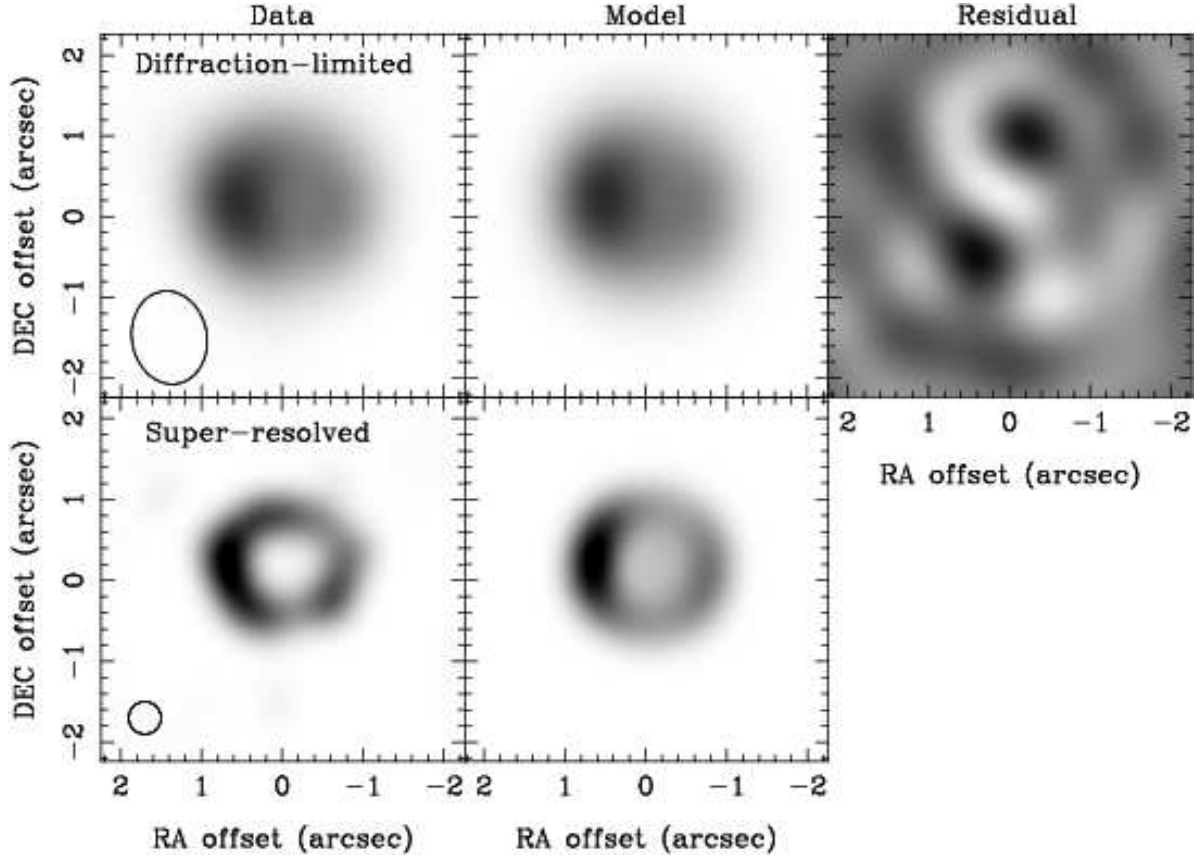


Fig. 8.— Super-resolved images at 9 GHz (*left column*) compared to the best-fit models (*middle column*) for the last epoch (2008.0). The scales are all linear, ranging from 10 to 40 mJy beam^{-1} for the diffraction-limited data and model images, and from 0 to 10 mJy beam^{-1} for the super-resolved images. As in Fig. 7, the dirty map of the residuals (*right column*), which are not deconvolved, has a linear scale ranging from from -1.5 to $1.5 \text{ mJy beam}^{-1}$. The synthesized beams are shown by the open ellipse and circle in the left column. Note that the model images shown here have been generated with identical u - v sampling as the data, while Fig. 6 was obtained by direct Fourier transform of the model visibility assuming a complete u - v coverage.

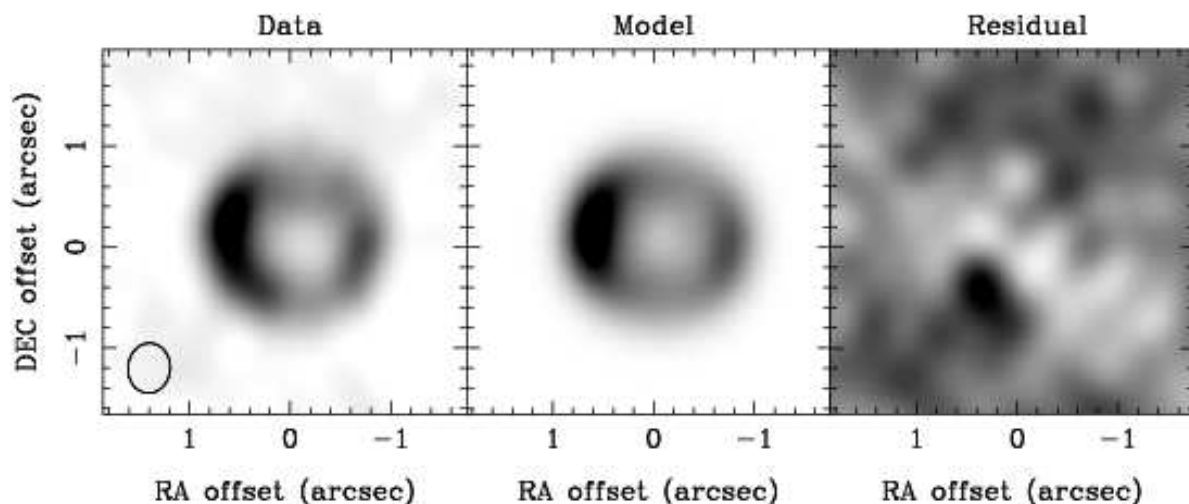


Fig. 9.— 18 GHz diffraction-limited images of the data, model and the residual map for epoch 2003.6 (Manchester et al. 2005). The synthesized beam is shown in the left panel. The linear scales range from 0 to 3.5 mJy beam⁻¹ in left two panels and from -0.5 to 0.5 mJy beam⁻¹ for the residual map. Note that no deconvolution has been applied to the latter.

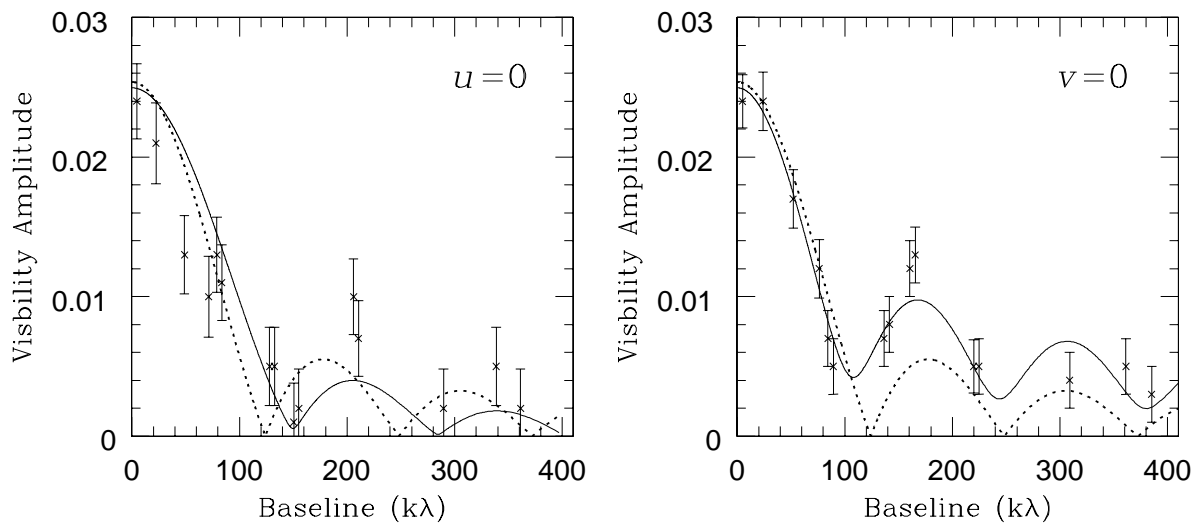


Fig. 10.— Similar plot as Fig. 4 for the 18 GHz observation at epoch 2003.6. Note that the left panel is actually a slice at 10° to the v -axis, due to the u - v coverage of the observation.

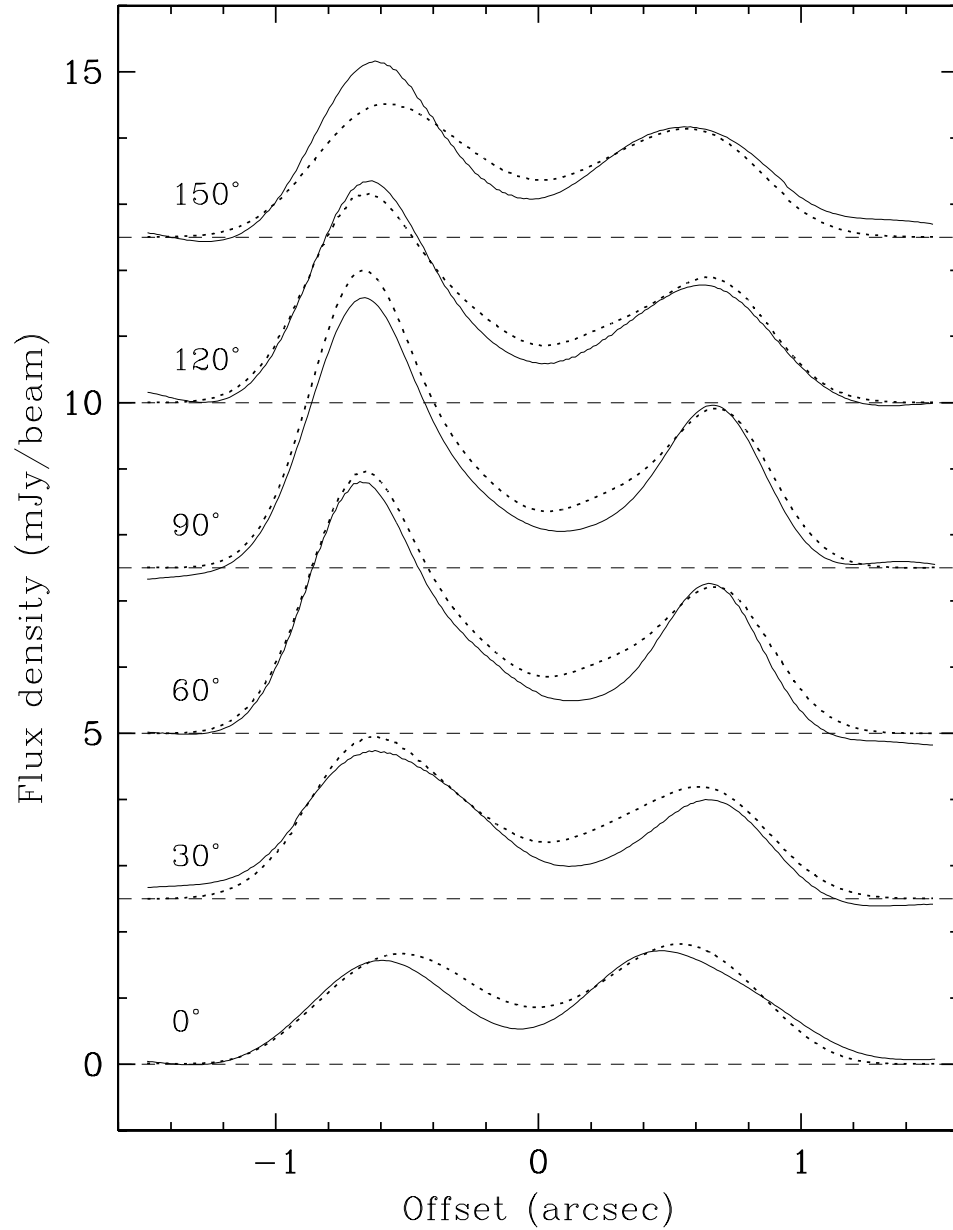


Fig. 11.— Slices through the 18 GHz diffraction-limited images in Fig. 9 at different position angles. The offset is radial from the torus center and is positive toward north and/or east. The data and model are shown by the solid and dotted lines respectively. The zero levels for each slice are shown by the dashed lines.

Table 1. Observational parameters for the datasets used in this study.

Observing date	Days since supernova	Array Configuration	Frequency (MHz)	Time on source (hr)	Epoch shown in Fig. 1 & 2 [†]
9 GHz Observations					
1992 Jan 14	1786	6B	8640	12	...
1992 Mar 20	1852	6A	8640	10	...
1992 Oct 21	2067	6C	8640, 8900	13	1992.9
1993 Jan 4	2142	6A	8640, 8900	9	1992.9
1993 Jan 5	2143	6A	8640, 8900	6	1992.9
1993 Jun 24	2313	6C	8640, 8900	8	1993.6
1993 Jul 1	2320	6C	8640, 8900	10	1993.6
1993 Oct 15	2426	6A	8640, 9024	17	1993.6
1994 Feb 16	2550	6B	8640, 9024	9	1994.4
1994 Jun 27-28	2681	6C	8640, 9024	21	1994.4
1994 Jul 1	2685	6A	8640, 9024	10	1994.4
1995 Jul 24	3073	6C	8640, 9024	12	1995.7
1995 Aug 29	3109	6D	8896, 9152	7	1995.7
1995 Nov 6	3178	6A	8640, 9024	9	1995.7
1996 Jul 21	3436	6C	8640, 9024	14	1996.7
1996 Sep 8	3485	6B	8640, 9024	13	1996.7
1996 Oct 5	3512	6A	8896, 9152	8	1996.7
1997 Nov 11	3914	6C	8512, 8896	7	1998.0
1998 Feb 18	4013	6A	8896, 9152	10	1998.0
1998 Feb 21	4016	6B	8512, 9024	7	1998.0
1998 Sep 13	4220	6A	8896, 9152	12	1998.9
1998 Oct 31	4268	6D	8502, 9024	11	1998.9
1999 Feb 12	4372	6C	8512, 8896	10	1999.7
1999 Sep 5	4577	6D	8768, 9152	11	1999.7
1999 Sep 12	4584	6A	8512, 8896	14	1999.7
2000 Sep 28	4966	6A	8512, 8896	10	2000.9
2000 Nov 12	5011	6C	8512, 8896	11	2000.9
2001 Nov 23	5387	6D	8768, 9152	8	2001.9
2002 Nov 19	5748	6A	8512, 8896	8	2003.0
2003 Jan 20	5810	6B	8512, 9024	9	2003.0
2003 Aug 1	6003	6D	8768, 9152	10	2003.6
2003 Dec 5	6129	6A	8512, 8896	9	2004.0
2004 Jan 15	6170	6A	8512, 8896	9	2004.0
2004 May 7	6283	6C	8512, 8896	9	2004.4
2005 Mar 25	6605	6A	8512, 8896	9	2005.2
2005 Jun 21	6693	6B	8512, 8896	9	2005.5
2006 Mar 28	6973	6C	8512, 8896	9	2006.2
2006 Jul 18	7085	6A	8512, 8896	9	2006.5
2006 Dec 8	7228	6B	8512, 9024	8	2006.9
2008 Jan 4	7620	6A	8512, 9024	11	2008.0
18 GHz Observations					
2003 Jul 31	6002	6D	17345, 19649	8	...
2004 May 6	6282	6C	17345, 19649	7	...

[†]Some datasets have been averaged together to generate the corresponding images in Fig. 1 and 2 for the listed epoch.

Table 2. Best-fit torus parameters for each epoch, with 1σ confidence intervals.

Day	f (mJy)	R (")	θ (°)	δ (%)	ϕ (°)	g (%)	χ^2/ν^\dagger	dof [§]
9 GHz Observations								
1786	$3.9^{+0.2}_{-0.2}$	$0.60^{+0.07}_{-0.04}$	70^{+10}_{-14}	162^{+19}_{-49}	188^{+20}_{-12}	83^{+16}_{-26}	1.8	2115
1852	$3.7^{+0.2}_{-0.2}$	$0.63^{+0.04}_{-0.08}$	46^{+19}_{-40}	108^{+66}_{-62}	57^{+54}_{-19}	76^{+24}_{-25}	3.7	1650
2067	$5.5^{+0.1}_{-0.2}$	$0.73^{+0.01}_{-0.07}$	56^{+2}_{-18}	108^{+72}_{-14}	143^{+3}_{-23}	99^{+1}_{-19}	4.3	3610
2142	$5.0^{+0.2}_{-0.2}$	$0.66^{+0.03}_{-0.02}$	63^{+3}_{-18}	81^{+101}_{-45}	142^{+13}_{-35}	45^{+54}_{-16}	17	2710
2143	$5.6^{+0.2}_{-0.1}$	$0.64^{+0.02}_{-0.01}$	$0.6^{+24}_{-0.4}$	1^{+37}_{-1}	92^{+25}_{-15}	39^{+13}_{-5}	16	1400
2313	$6.7^{+0.1}_{-0.1}$	$0.62^{+0.01}_{-0.01}$	33^{+5}_{-8}	1^{+33}_{-1}	83^{+9}_{-11}	40^{+7}_{-3}	3.6	2910
2320	$7.0^{+0.2}_{-0.2}$	$0.67^{+0.02}_{-0.03}$	31^{+8}_{-15}	63^{+33}_{-48}	78^{+12}_{-8}	41^{+9}_{-7}	4.5	2970
2426	$6.7^{+0.1}_{-0.1}$	$0.690^{+0.009}_{-0.008}$	53^{+2}_{-3}	36^{+19}_{-35}	75^{+9}_{-8}	43^{+5}_{-15}	5.2	4380
2550	$6.5^{+0.2}_{-0.2}$	$0.73^{+0.02}_{-0.06}$	57^{+3}_{-25}	91^{+8}_{-23}	133^{+9}_{-27}	81^{+5}_{-15}	7.5	3000
2681	$8.4^{+0.1}_{-0.1}$	$0.672^{+0.005}_{-0.005}$	46^{+1}_{-2}	23^{+17}_{-23}	78^{+6}_{-7}	35^{+4}_{-2}	6.0	6150
2685	$8.1^{+0.1}_{-0.1}$	$0.665^{+0.007}_{-0.007}$	52^{+2}_{-2}	1^{+16}_{-1}	106^{+8}_{-10}	37^{+3}_{-2}	5.7	3264
3073	$11.1^{+0.2}_{-0.2}$	$0.671^{+0.008}_{-0.008}$	32^{+3}_{-4}	52^{+11}_{-13}	80^{+5}_{-4}	41^{+2}_{-2}	5.6	2670
3109	$9.7^{+0.4}_{-0.3}$	$0.633^{+0.02}_{-0.005}$	16^{+26}_{-15}	1^{+17}_{-5}	75^{+12}_{-6}	43^{+5}_{-3}	17	1606
3178	$11.7^{+0.1}_{-0.1}$	$0.685^{+0.005}_{-0.004}$	44^{+2}_{-2}	$0.4^{+3}_{-0.3}$	94^{+4}_{-4}	$38.0^{+1.4}_{-1.2}$	4.0	3450
3436	$15.2^{+0.1}_{-0.1}$	$0.705^{+0.004}_{-0.003}$	$46.3^{+0.9}_{-1.0}$	26^{+8}_{-14}	95^{+3}_{-4}	$41.9^{+1.4}_{-1.2}$	4.9	4345
3485	$15.4^{+0.1}_{-0.1}$	$0.707^{+0.004}_{-0.004}$	$50.1^{+1.0}_{-1.0}$	$0.4^{+7}_{-0.29}$	102^{+3}_{-3}	$43.3^{+1.4}_{-1.3}$	5.2	4710
3512	$15.4^{+0.1}_{-0.1}$	$0.708^{+0.005}_{-0.006}$	$51.1^{+1.2}_{-1.4}$	$0.1^{+25}_{-0.1}$	94^{+5}_{-5}	42^{+3}_{-2}	3.3	2640
3914	$17.6^{+0.2}_{-0.2}$	$0.694^{+0.007}_{-0.006}$	41^{+2}_{-2}	$0.04^{+0.5}_{-0.94}$	112^{+4}_{-5}	39^{+2}_{-2}	2.4	1280
4013	$19.1^{+0.1}_{-0.1}$	$0.754^{+0.004}_{-0.004}$	$45.5^{+1.0}_{-1.0}$	$0.3^{+0.3}_{-0.3}$	105^{+2}_{-2}	$45.1^{+1.2}_{-1.0}$	3.0	2838
4016	$18.7^{+0.1}_{-0.1}$	$0.745^{+0.005}_{-0.004}$	$49.4^{+1.1}_{-1.1}$	$0.1^{+0.1}_{-0.1}$	103^{+3}_{-3}	$45.7^{+1.1}_{-1.0}$	3.1	2520
4220	$20.2^{+0.1}_{-0.1}$	$0.729^{+0.003}_{-0.004}$	$42.6^{+0.9}_{-1.0}$	6^{+8}_{-5}	100^{+2}_{-2}	$37.6^{+0.8}_{-0.8}$	2.2	2963
4268	$21.8^{+0.3}_{-0.3}$	$0.736^{+0.004}_{-0.004}$	$40.0^{+1.0}_{-1.0}$	30^{+8}_{-15}	107^{+2}_{-2}	$38.0^{+0.9}_{-0.8}$	7.3	3870
4372	$22.9^{+0.2}_{-0.2}$	$0.727^{+0.004}_{-0.005}$	$36.6^{+1.1}_{-1.1}$	24^{+10}_{-9}	114^{+2}_{-2}	$37.5^{+0.8}_{-0.7}$	3.6	3540
4577	$23.9^{+0.3}_{-0.2}$	$0.757^{+0.005}_{-0.005}$	$39.9^{+0.8}_{-1.1}$	22^{+9}_{-19}	103^{+2}_{-2}	$39.4^{+0.7}_{-0.9}$	7.0	3450
4584	$25.2^{+0.09}_{-0.08}$	$0.747^{+0.002}_{-0.002}$	$41.4^{+0.7}_{-0.7}$	$0.4^{+0.1}_{-0.3}$	109^{+2}_{-2}	$38.5^{+0.6}_{-0.6}$	2.9	4230
4966	$29.4^{+0.05}_{-0.06}$	$0.764^{+0.002}_{-0.002}$	$40.0^{+0.6}_{-0.7}$	$0.3^{+0.3}_{-0.2}$	$108.5^{+1.3}_{-1.3}$	$39.6^{+0.5}_{-0.5}$	1.3	50697
5011	$33.0^{+0.07}_{-0.08}$	$0.776^{+0.002}_{-0.002}$	$43.4^{+0.5}_{-0.7}$	$0.1^{+0.7}_{-0.02}$	$104.9^{+1.4}_{-1.3}$	$40.1^{+0.6}_{-0.5}$	1.4	50539
5387	$34.1^{+0.1}_{-0.1}$	$0.789^{+0.003}_{-0.003}$	$40.7^{+1.0}_{-0.9}$	$0.01^{+3.4}_{-0.01}$	$108.2^{+1.1}_{-1.2}$	$41.4^{+0.5}_{-0.6}$	1.6	39612
5748	$41.7^{+0.06}_{-0.08}$	$0.811^{+0.001}_{-0.002}$	$43.0^{+0.5}_{-0.5}$	$0.10^{+0.3}_{-0.05}$	$103.0^{+1.2}_{-0.9}$	$40.4^{+0.3}_{-0.5}$	1.3	39000
5810	$42.5^{+0.07}_{-0.07}$	$0.815^{+0.001}_{-0.001}$	$42.2^{+0.5}_{-0.4}$	$0.001^{+0.4}_{-0.001}$	$118.1^{+0.9}_{-0.9}$	$43.2^{+0.4}_{-0.5}$	1.6	46020
6003	$46.5^{+0.1}_{-0.08}$	$0.813^{+0.003}_{-0.001}$	$38.8^{+1.0}_{-0.4}$	$0.06^{+3.7}_{-0.01}$	$100.3^{+2}_{-0.04}$	$38.2^{+0.5}_{-0.3}$	1.6	45000
6129	$52.8^{+0.08}_{-0.07}$	$0.833^{+0.002}_{-0.002}$	$41.9^{+0.6}_{-0.4}$	$0.01^{+0.3}_{-0.01}$	$107.7^{+0.9}_{-1.0}$	$42.2^{+0.4}_{-0.4}$	1.3	46020
6170	$54.0^{+0.1}_{-0.07}$	$0.831^{+0.002}_{-0.001}$	$41.4^{+0.6}_{-0.4}$	$0.17^{+2.4}_{-0.14}$	$108.1^{+1.3}_{-0.6}$	$38.8^{+0.5}_{-0.3}$	1.5	43680
6283	$53.6^{+0.08}_{-0.06}$	$0.829^{+0.001}_{-0.001}$	$39.0^{+0.5}_{-0.5}$	$0.16^{+1.0}_{-0.11}$	$107.3^{+1.0}_{-0.6}$	$38.7^{+0.4}_{-0.3}$	1.5	44850
6605	$61.3^{+0.1}_{-0.1}$	$0.844^{+0.002}_{-0.002}$	$37.7^{+0.5}_{-0.6}$	$0.19^{+2.1}_{-0.14}$	$108.2^{+1.0}_{-0.6}$	$39.0^{+0.3}_{-0.3}$	2.9	42900
6693	$62.7^{+0.07}_{-0.08}$	$0.858^{+0.001}_{-0.001}$	$42.2^{+0.4}_{-0.4}$	$0.11^{+0.8}_{-0.06}$	$100.6^{+0.9}_{-0.9}$	$35.8^{+0.3}_{-0.3}$	1.5	39000
6973	$73.7^{+0.08}_{-0.07}$	$0.881^{+0.001}_{-0.001}$	$43.8^{+0.4}_{-0.3}$	$0.01^{+3.6}_{-0.01}$	$116.4^{+0.6}_{-0.7}$	$41.8^{+0.4}_{-0.3}$	1.5	40365
7085	$77.1^{+0.07}_{-0.09}$	$0.872^{+0.001}_{-0.002}$	$38.8^{+0.4}_{-0.5}$	$0.03^{+0.9}_{-0.001}$	$110.5^{+0.5}_{-0.6}$	$39.5^{+0.3}_{-0.3}$	1.5	29120
7228	$82.4^{+0.10}_{-0.09}$	$0.874^{+0.002}_{-0.001}$	$39.4^{+0.5}_{-0.4}$	$0.07^{+6.8}_{-0.04}$	$107.3^{+0.5}_{-0.6}$	$39.1^{+0.3}_{-0.2}$	1.4	35685
7620	$93.5^{+0.10}_{-0.10}$	$0.893^{+0.001}_{-0.001}$	$41.8^{+0.7}_{-0.4}$	$0.03^{+6.1}_{-0.00}$	$103.7^{+0.5}_{-0.5}$	$38.6^{+0.3}_{-0.3}$	1.3	42900
18 GHz Observations								
6002	$25.1^{+0.08}_{-0.07}$	$0.80^{+0.002}_{-0.002}$	$32.1^{+0.6}_{-0.5}$	$0.03^{+0.3}_{-0.03}$	$99.1^{+1.4}_{-1.4}$	$36.5^{+0.6}_{-0.6}$	0.7	42939
6282	$24.3^{+0.10}_{-0.09}$	$0.81^{+0.002}_{-0.002}$	$26.9^{+0.6}_{-0.8}$	10^{+6}_{-9}	$108.2^{+1.5}_{-1.4}$	$36.2^{+0.9}_{-0.8}$	1.0	31200

[†]The χ^2 values include the statistical errors only, while the uncertainties in the parameters include the systematic errors (see text).

[§]Before 2000, all 13 frequency channels in the data were averaged to boost the signal and to reduce the computing time.

Table 3. Best-fit parameters for the shell fit and shell+2 points fit.

Day	Fit to shell alone			Fit to shell + 2 points											
	f_{shell} (mJy)	R ('')	χ^2/ν	f_{shell} (mJy)	R ('')	f_1 (mJy)	δRA_1 ('')	δDec_1 ('')	f_2 (mJy)	δRA_2 ('')	δDec_2 ('')	f_{ratio}^\dagger	d_1/R^\S	d_2/R^\S	χ^2/ν
1786	3.8	0.67	1.8	2.5	0.97	1.2	-0.04	-0.09	0.4	-0.83	-0.05	1.5	0.10	0.86	1.8
1852	3.6	0.64	3.7	2.6	0.57	0.5	-0.02	-0.57	0.5	-0.88	-0.02	1.0	1.00	1.54	3.7
2067	5.3	0.67	4.4	4.0	0.81	1.1	0.17	-0.03	0.3	-0.71	-0.34	1.3	0.21	0.98	4.3
2142	4.9	0.67	17	4.1	0.76	0.7	0.17	-0.05	0.2	-0.44	-0.04	1.2	0.23	0.58	17
2143	5.6	0.63	16	4.2	0.67	1.1	0.41	-0.06	0.3	-0.76	-0.10	1.3	0.61	1.15	16
2313	6.7	0.62	3.6	5.1	0.64	1.2	0.36	-0.14	0.5	-0.74	-0.04	1.2	0.61	1.15	3.6
2320	7.0	0.67	4.5	5.3	0.72	1.2	0.36	-0.07	0.5	-0.69	0.14	1.2	0.51	0.97	4.5
2426	6.6	0.67	5.3	5.3	0.76	1.1	0.31	-0.07	0.3	-0.48	0.10	1.3	0.42	0.64	5.2
2550	6.3	0.71	7.5	4.9	0.76	0.6	0.77	0.61	0.9	0.29	0.03	0.9	1.29	0.39	7.5
2681	8.4	0.66	6.1	6.7	0.72	1.3	0.30	0.00	0.5	-0.70	0.11	1.2	0.41	0.98	6.0
2685	8.0	0.66	5.7	6.5	0.70	1.2	0.30	-0.07	0.4	-0.78	0.11	1.2	0.44	1.12	5.6
3073	11	0.69	5.9	8.8	0.70	1.8	0.45	-0.06	0.5	-0.86	-0.10	1.3	0.66	1.24	5.6
3109	10	0.69	17	6.7	0.66	2.2	0.43	-0.03	0.7	-0.59	0.07	1.4	0.66	0.90	17
3178	12	0.69	4.2	9.2	0.73	2.0	0.39	-0.07	0.5	-0.65	-0.04	1.3	0.55	0.90	4.0
3436	15	0.69	5.3	12	0.76	2.5	0.35	-0.04	0.6	-0.72	0.08	1.3	0.46	0.95	4.9
3485	15	0.69	5.4	13	0.76	2.5	0.36	-0.01	0.3	-0.64	0.03	1.3	0.47	0.84	5.1
3512	15	0.69	3.5	12	0.77	2.6	0.37	-0.03	0.4	-0.58	0.15	1.3	0.48	0.77	3.3
3914	17	0.72	2.8	14	0.76	2.9	0.43	-0.08	0.7	-0.82	0.32	1.3	0.57	1.15	2.4
4013	19	0.74	3.6	15	0.80	3.2	0.41	0.00	0.4	-0.70	-0.09	1.3	0.51	0.88	3.0
4016	19	0.74	3.6	14	0.77	3.5	0.41	0.01	0.7	-0.62	0.23	1.4	0.54	0.85	3.0
4220	20	0.73	2.7	16	0.77	3.2	0.41	-0.02	0.9	-0.79	0.05	1.3	0.54	1.03	2.2
4268	22	0.73	7.9	17	0.80	3.6	0.38	-0.02	1.0	-0.77	-0.07	1.3	0.48	0.97	7.3
4372	23	0.75	4.3	18	0.78	3.6	0.40	-0.04	1.3	-0.83	-0.08	1.2	0.52	1.07	3.6
4577	24	0.76	7.8	19	0.81	4.0	0.42	0.00	1.0	-0.78	0.02	1.3	0.51	0.96	7.0
4584	25	0.74	3.6	20	0.79	4.0	0.43	-0.03	1.1	-0.80	-0.07	1.3	0.55	1.02	2.8
4966	29	0.76	1.4	23	0.81	4.8	0.43	-0.03	1.4	-0.83	-0.07	1.3	0.54	1.03	1.3
5011	33	0.77	1.5	27	0.82	5.2	0.43	-0.03	1.2	-0.81	-0.04	1.3	0.53	0.99	1.4
5387	34	0.80	1.7	27	0.83	5.5	0.45	-0.03	1.4	-0.83	-0.08	1.3	0.54	1.00	1.6
5748	41	0.81	1.5	34	0.85	6.5	0.46	-0.02	1.6	-0.87	-0.01	1.3	0.55	1.02	1.3
5810	42	0.82	1.7	34	0.85	6.4	0.47	0.01	1.6	-0.92	-0.14	1.3	0.55	1.09	1.6
6003	46	0.83	1.8	38	0.85	7.1	0.50	-0.03	1.8	-0.88	-0.05	1.3	0.59	1.03	1.6
6129	53	0.84	1.5	42	0.88	8.6	0.47	-0.02	1.8	-0.85	-0.07	1.3	0.54	0.97	1.3
6170	54	0.85	1.7	44	0.87	8.4	0.50	-0.02	2.0	-0.84	-0.08	1.3	0.57	0.97	1.5
6283	53	0.84	1.8	44	0.87	7.8	0.50	-0.01	1.9	-0.96	-0.09	1.2	0.58	1.11	1.5
6605	61	0.86	3.3	49	0.88	9.5	0.51	0.00	2.6	-0.91	-0.07	1.3	0.58	1.04	2.9
6693	62	0.87	1.8	52	0.88	8.6	0.54	-0.01	2.5	-1.00	-0.03	1.2	0.61	1.13	1.5
6973	73	0.90	1.9	60	0.92	10	0.48	0.05	2.8	-0.94	-0.07	1.2	0.53	1.02	1.5
7085	77	0.89	2.3	64	0.92	11	0.52	0.02	2.7	-0.92	-0.11	1.2	0.57	1.01	1.6
7228	82	0.90	2.1	67	0.92	12	0.54	0.01	2.7	-0.92	-0.25	1.3	0.58	1.03	1.5
7620	93	0.89	1.7	79	0.92	12	0.55	0.01	2.9	-0.99	-0.10	1.2	0.59	1.08	1.4

Note. — f_{shell} and R are the flux density and radius of the thin spherical shell. The point source in the east has a flux density f_1 and is offset by δRA_1 and δDec_1 from the shell center, in RA and Dec respectively. Similarly, f_2 , δRA_2 and δDec_2 are for the point source in the west.

[†]The flux ratio between the eastern and western lobes is defined as $f_{\text{ratio}} = \frac{f_{\text{shell}}/2 + f_1}{f_{\text{shell}}/2 + f_2}$.

[§]The offset from the shell center to the point source is defined as $d_i = \sqrt{(\delta\text{RA}_i)^2 + (\delta\text{Dec}_i)^2}$.